

Polycrystal Plasticity Modeling of Nickel-based Superalloy IN 617 Subjected to Cyclic Loading at High Temperature

Xiang Zhang and Caglar Oskay*

*Department of Civil and Environmental Engineering
Vanderbilt University
Nashville, TN 37235*

Abstract

A crystal plasticity finite element (CPFE) model considering isothermal, large deformation and cyclic loading conditions has been formulated and employed to investigate the mechanical response of a nickel-based alloy at high temperature. The investigations focus on fatigue and creep-fatigue hysteresis response of IN 617 subjected to fatigue and creep-fatigue cycles. A new slip resistance evolution equation is proposed to account for cyclic transient features induced by solute drag creep that occur in IN 617 at 950°C. The crystal plasticity model parameters are calibrated against the experimental fatigue and creep-fatigue data based on an optimization procedure that relies on a surrogate modeling (i.e., Gaussian Process) technique to accelerate multi-parameter optimizations. The model predictions are validated against experimental data, which demonstrates the capability of the proposed model in capturing the hysteresis behavior for various hold times and strain ranges in the context of fatigue and creep-fatigue loading.

Keywords: Crystal Plasticity; Nickel-based Superalloy; Fatigue; Creep-Fatigue; Solute-Drag Creep

1 Introduction

Nickel-based alloys are widely used as structural materials for turbine engine blades, aircraft engine components, and high temperature power plant steam generators due to their excep-

*Corresponding author address: VU Station B#351831, 2301 Vanderbilt Place, Nashville, TN 37235. Email: caglar.oskay@vanderbilt.edu

tional combination of high temperature strength and creep resistance. In particular, IN 617 is a candidate structural material for very high temperature reactor (VHTR) intermediate heat exchangers [46]. Under these conditions, the material experiences extreme thermal (up to 950°C) and mechanical loadings, including fatigue and creep-fatigue induced by the startup and shutdown cycles. Prediction of failure and life of this alloy under high temperature creep-fatigue conditions is therefore a critical concern. Developing a computational model that incorporates the underlying physics of the plastic deformation, which can lead to the ability to capture the response in cyclic loading, and ultimately, life prediction capability is of significant interest.

IN 617 is a solid solution strengthened nickel-based alloy with coarse Cr and Mo carbides as well as small amount of Ti carbonitrides [49]. γ' phase also exists at relatively low temperatures, but becomes unstable above 650°C [26, 4]. Tensile tests of IN 617 at various temperatures and strain ranges have been studied and it generally exhibits strong temperature and strain rate dependence [52, 40], as well as orientation (between loading direction and sample rolling direction) dependence [32]. Strain controlled fatigue and creep-fatigue tests of IN 617 at 850°C and 950°C have been experimentally studied by several researchers over various strain ranges and hold times [13, 54, 10, 53]. Wright et al. [54] found that under fatigue loading at 850°C, IN 617 deforms by a plastic flow mechanism and shows cyclic hardening, while at 950°C the alloy exhibits softening induced by solute-drag creep. Introduction of a tensile hold in the creep-fatigue tests significantly decreases the fatigue life compared to that under pure fatigue loading. Microstructure examinations showed failure is controlled by intergranular fracture under creep-fatigue loading, while transgranular cracking dominates when subjected to pure fatigue loads [10]. Further, the microstructure is marked by the formation of dislocation substructures during creep-fatigue testing, which influences the dislocation density and motion within grains [8]. The sensitivity of fatigue and creep-fatigue deformation and failure mechanisms to environmental (e.g., temperature) conditions points to the influence of microstructure on the life of these alloys.

A few viscoplastic constitutive models [43, 38, 33] based on the phenomenological constitutive theories of Robinson [41] and Chaboche [12] have been developed to capture the cyclic response of IN 617 at high temperatures. Chen et al. [13] utilized frequency-modified tensile hysteresis energy to predict the low cycle fatigue and creep-fatigue life of IN 617. While these phenomenological models are successful in capturing the stress-strain loops, they do not provide a direct account of microstructural heterogeneities and their interactions, which may affect

the overall long term behavior. Crystal plasticity finite element method (CPFE) is an alternative modeling approach, which is based on full resolution of the representative microstructure of the material. Since its inception [34, 35], CPFE has been developed into a robust numerical strategy to capture the grain level anisotropic deformation of metals and alloys at various loading conditions (see, e.g., Roters et al. [42] for an extensive review). Under the assumption that slip is the dominant carrier of plastic deformation, stress is resolved onto individual slip systems inherent to the lattice structure of the material, which drives dislocation glide and the accumulation of plastic strain. More recent investigations incorporated dislocation climb mechanisms [23], as well as deformation twinning [19] into the CPFE framework to study the high temperature behavior of alloys. A number of numerical investigations employed CPFE to study the cyclic response of various alloys, either to capture the stress-strain response, crack initiation or failure life prediction [57, 58, 50, 1]. Simulations of the cyclic behavior of nickel-based alloys at intermediate and high temperatures have been performed in Refs. [6, 5, 24], which demonstrated the capability of CPFE to capture hysteresis loops as well as the stress relaxation phenomenon.

Prior experimental studies on the fatigue and creep-fatigue behavior of IN 617 identified a prominent drop in the flow stress (i.e., apparent softening) in the first cycle of both fatigue and creep-fatigue tests. In creep-fatigue testing of IN 617 at 950°C, the apparent softening recurs at every cycle after strain holds as well. These stress drops have been attributed to solute-drag creep [54], which occurs due to the dynamic interactions between dislocations and the solute atoms ([45, 47]). While models of solute-drag creep have been proposed in the literature [47], to the best of the authors' knowledge, the modeling of transient phenomena induced by solute-drag creep has not been included into the CPFE framework.

In this manuscript, a crystal plasticity model is developed to idealize the fatigue and creep-fatigue cycles of IN 617 at high temperature environment. The CPFE model that incorporates isothermal deformation behavior of the alloy as well as the large deformation kinematics has been formulated, implemented and validated. The proposed CPFE model includes a new slip resistance evolution law that accounts for the solute-drag creep and can capture the transient softening effects observed under fatigue and creep-fatigue tests. Model parameters in the CPFE model are calibrated by employing a model calibration procedure that is based on Gaussian Process modeling to accelerate the process. Simulations were performed using polycrystal morphologies generated using experimental (i.e., EBSD) data along with the calibrated CPFE

model. The simulation predictions were found to be in good agreement with all fatigue and creep-fatigue tests at different strain ranges and hold times. **The proposed model, although calibrated for 950 °C, is expected to apply within a range of temperature between approximately 900-1000 °C. Within this range, the microstructure of IN 617 is largely free of γ' precipitates with a relatively stable microstructure [26, 4].**

The remainder of this manuscript is organized as follows: Section 2 provides an overview of the crystal plasticity constitutive relations as well as the detailed flow rule and evolution equations for IN 617, followed by the numerical implementation details. Section 3 describes the microstructure reconstruction and the calibration process. Section 4 presents the validation of the proposed CPFE deformation model of IN 617 by comparing the simulated response to experiments performed at INL.

2 The crystal plasticity model

A comprehensive review of various crystal plasticity models is provided in Roters et al. [42]. Twinning and dislocation slip have been the most studied deformation mechanism in the context of crystal plasticity and implementation into CPFE framework is readily available. Mechanical twinning preferentially occurs in coarse-grained crystalline metals with low symmetry at low temperature and high strain rate [56, 15, 21, 2]. Furthermore, no significant deformation twining has been reported in the experimental literature for alloy 617 at high temperatures. While evidence of dislocation climb of IN 617 at temperatures between 850 and 1050°C has been reported by Wen [51], it is also pointed out that dislocation glide is still the dominant deformation mechanism. On the other hand, dislocation climb modeling under the context of CPFE has been very recent [16, 23]. In this study, a simplifying assumption is made, where all plastic deformation is modeled as a consequence of dislocation glide. Full traction continuity is assumed along each grain boundary (i.e., the modeling is valid up to the onset of damage initiation). The large deformation formulation is based on the framework of Marin and Dawson [27, 28] and a brief overview of this framework is provided herein for completeness. The kinematic theory implemented in the current CPFE model falls within the theory of Taylor [48] and Hill and Rice [18].

Consider a body that occupies the reference domain \mathbb{B}_0 that corresponds to the initial state of the polycrystal microstructure. The current domain is denoted by \mathbb{B} as shown in Fig. 1.

The motion of the body is described using the deformation map, $\phi(\mathbf{X}, t)$:

$$\mathbf{x} = \phi(\mathbf{X}, t); \quad \mathbf{X} \in \mathbb{B}_0, \quad \mathbf{x} \in \mathbb{B} \quad (1)$$

where, \mathbf{x} and \mathbf{X} denote the position vectors in the current and reference (initial) configurations, respectively. The displacement field, $\mathbf{u}(\mathbf{X}, t)$, is then expressed as:

$$\mathbf{u}(\mathbf{X}, t) = \phi(\mathbf{X}, t) - \mathbf{X}; \quad \mathbf{X} \in \mathbb{B}_0 \quad (2)$$

The deformation gradient, $\mathbf{F} = \partial\phi/\partial\mathbf{X}$, is expressed using the classical multiplicative split into elastic (\mathbf{F}^e) and plastic (\mathbf{F}^p) contributions as:

$$\mathbf{F} = \mathbf{F}^e \cdot \mathbf{F}^p \quad (3)$$

Polar decomposition of the elastic part of the deformation tensor into the left elastic stretch tensor, \mathbf{V}^e , and the orthogonal rotation tensor, \mathbf{R}^e (i.e., $\det(\mathbf{R}^e) = 1$ and $\mathbf{R}^{e-1} = \mathbf{R}^{eT}$), allows Eq. (3) to be expanded as:

$$\mathbf{F} = \mathbf{V}^e \cdot \mathbf{F}^*, \quad \mathbf{F}^* = \mathbf{R}^e \cdot \mathbf{F}^p \quad (4)$$

in which, superscripts -1 and T denotes tensor inverse and transpose, respectively. The above decomposition allows the introduction of two intermediate configurations denoted as $\bar{\mathbb{B}}$ and $\tilde{\mathbb{B}}$ between the original configuration, \mathbb{B}_0 , and the current configuration, \mathbb{B} , as shown in Fig. 1. In what follows, an overbar or tilde indicates the value of a variable at the corresponding intermediate configuration. The current formulation operates in the intermediate configuration, $\tilde{\mathbb{B}}$, obtained by elastically unloading from the current configuration, \mathbb{B} . \mathbf{F}^p is related to the dislocations on crystallographic planes and \mathbf{V}^e is a pure elastic stretching of the lattice, both of which do not change the crystal orientation. \mathbf{R}^e defines the rotation and the reorientation of the grains. By this approach, it is straightforward to incorporate crystal elasticity to CPFE. This is in contrast to formulations based on a single intermediate configuration, where the behavior is often idealized as rigid viscoplastic.

Each slip system α is uniquely defined by its Schmid tensor $\mathbf{Z}^\alpha = \mathbf{m}^\alpha \otimes \mathbf{n}^\alpha$, where \mathbf{n}^α and \mathbf{m}^α are the unit vectors normal to the slip plane and along the slip direction, respectively.

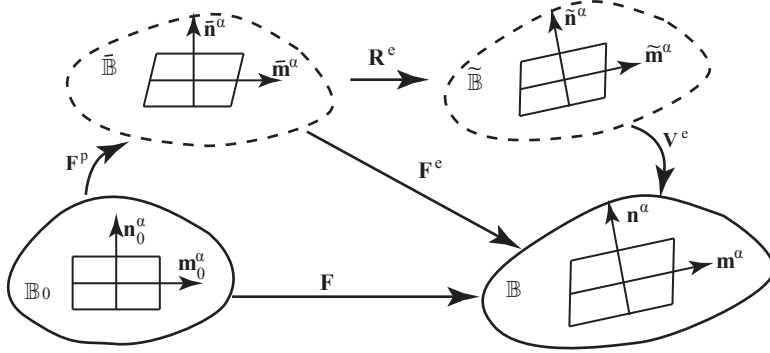


Figure 1: Kinematics of the deformation.

Since the lattice orientation is affected only by \mathbf{R}^e :

$$\bar{\mathbf{n}}^\alpha = \mathbf{n}_0^\alpha; \quad \bar{\mathbf{m}}^\alpha = \mathbf{m}_0^\alpha; \quad \mathbf{n}^\alpha = \tilde{\mathbf{n}}^\alpha; \quad \mathbf{m}^\alpha = \tilde{\mathbf{m}}^\alpha \quad (5)$$

The grain orientation is updated using the rotation tensor \mathbf{R}^e :

$$\tilde{\mathbf{n}}^\alpha = \mathbf{R}^e \cdot \bar{\mathbf{n}}^\alpha; \quad \tilde{\mathbf{m}}^\alpha = \mathbf{R}^e \cdot \bar{\mathbf{m}}^\alpha \quad (6)$$

which, describes the texture evolution during the deformation process.

The plastic velocity gradients $\bar{\mathbf{L}}^p$ and $\tilde{\mathbf{L}}^p$ in the intermediate configurations $\bar{\mathbb{B}}$ and $\tilde{\mathbb{B}}$, respectively, are expressed as:

$$\bar{\mathbf{L}}^p = \dot{\mathbf{F}}^p \cdot \mathbf{F}^{p-1} = \sum_{\alpha=1}^N \dot{\gamma}^\alpha \bar{\mathbf{m}}^\alpha \otimes \bar{\mathbf{n}}^\alpha \quad (7)$$

$$\tilde{\mathbf{L}}^p = \dot{\mathbf{F}}^* \cdot \mathbf{F}^{*-1} = \tilde{\boldsymbol{\Omega}}^e + \mathbf{R}^e \cdot \bar{\mathbf{L}}^p \cdot \mathbf{R}^{eT} \quad (8)$$

where, $\tilde{\boldsymbol{\Omega}}^e = \dot{\mathbf{R}}^e \cdot \mathbf{R}^{eT}$ denotes the spin of the lattice in configuration $\tilde{\mathbb{B}}$, and possesses skew symmetry [3]. The velocity gradient \mathbf{L} in the current configuration \mathbb{B} is expressed as:

$$\mathbf{L} = \dot{\mathbf{F}} \cdot \mathbf{F}^{-1} = \dot{\mathbf{V}}^e \cdot \mathbf{V}^{e-1} + \mathbf{V}^e \cdot \tilde{\mathbf{L}}^p \cdot \mathbf{V}^{e-1} \quad (9)$$

The velocity gradients \mathbf{L} , $\bar{\mathbf{L}}^p$ and $\tilde{\mathbf{L}}^p$ are decomposed into their symmetric (\mathbf{D} , $\bar{\mathbf{D}}^p$, $\tilde{\mathbf{D}}^p$) and skew (\mathbf{W} , $\bar{\mathbf{W}}^p$, $\tilde{\mathbf{W}}^p$) components as:

$$\mathbf{L} = \mathbf{D} + \mathbf{W}, \quad \bar{\mathbf{L}}^p = \bar{\mathbf{D}}^p + \bar{\mathbf{W}}^p, \quad \tilde{\mathbf{L}}^p = \tilde{\mathbf{D}}^p + \tilde{\mathbf{W}}^p \quad (10)$$

which, together with Eqs. (7) and (8), yields:

$$\bar{\mathbf{D}}^p = \sum_{\alpha=1}^N \dot{\gamma} (\bar{\mathbf{m}}^\alpha \otimes \bar{\mathbf{n}}^\alpha)_S, \quad \bar{\mathbf{W}}^p = \sum_{\alpha=1}^N \dot{\gamma} (\bar{\mathbf{m}}^\alpha \otimes \bar{\mathbf{n}}^\alpha)_A \quad (11)$$

$$\tilde{\mathbf{D}}^p = \mathbf{R}^e \cdot \bar{\mathbf{D}}^p \cdot \mathbf{R}^e, \quad \tilde{\mathbf{W}}^p = \tilde{\boldsymbol{\Omega}}^e + \mathbf{R}^e \cdot \bar{\mathbf{W}}^p \cdot \mathbf{R}^{eT} \quad (12)$$

where, the subscripts S and A indicate the symmetric and skew (anti-symmetry) components, respectively (i.e., $(\cdot)_S = ((\cdot) + (\cdot)^T)/2$; $(\cdot)_A = ((\cdot) - (\cdot)^T)/2$).

The stress-strain relationship of the lattice is expressed as:

$$\tilde{\mathbf{S}} = \tilde{\mathbb{C}} : \tilde{\mathbf{E}}^e \quad (13)$$

where, $\tilde{\mathbb{C}}$ is the fourth order anisotropic crystal elasticity tensor, $\tilde{\mathbf{S}}$ the 2nd Piola-Kirchhoff stress in $\tilde{\mathbb{B}}$, and $\tilde{\mathbf{E}}^e$ the Green strain tensor relative to $\tilde{\mathbb{B}}$, which takes the form:

$$\tilde{\mathbf{E}}^e = \frac{1}{2} (\mathbf{V}^{eT} \cdot \mathbf{V}^e - \mathbf{I}) \quad (14)$$

in which, \mathbf{I} is the second order identity tensor. $\tilde{\mathbf{S}}$ relates with the Cauchy stress, $\boldsymbol{\sigma}$, and Kirchhoff stress, $\boldsymbol{\tau}$, in the current configuration through the transformations [3]:

$$\tilde{\mathbf{S}} = \mathbf{V}^{-e} \cdot \boldsymbol{\tau} \cdot \mathbf{V}^{-eT} = \det(\mathbf{V}^e) \mathbf{V}^{-e} \cdot \boldsymbol{\sigma} \cdot \mathbf{V}^{-eT} \quad (15)$$

The elastic lattice strains are generally orders of magnitude less than the plastic strains in many applications of interest, hence the small elastic strains assumption is adopted for simplicity [27, 28]:

$$\mathbf{V}^e = \mathbf{I} + \boldsymbol{\epsilon}^e, \quad \|\boldsymbol{\epsilon}^e\| \ll 1 \quad (16)$$

in which, $\boldsymbol{\epsilon}^e$ denotes elstic strains. Time differentiation and inverse operation yield:

$$\dot{\mathbf{V}}^e = \dot{\boldsymbol{\epsilon}}^e, \quad \mathbf{V}^{e-1} = \mathbf{I} - \boldsymbol{\epsilon}^e \quad (17)$$

Substituting Eqs. (16) and (17) into Eq. (13)-(15), dropping high order terms of $\boldsymbol{\epsilon}^e$, and neglecting terms such as $(\bullet)\boldsymbol{\epsilon}^e$ and $\boldsymbol{\epsilon}^e(\bullet)$ in comparison to (\bullet) , the stress-strain

relationship is expressed as:

$$\boldsymbol{\tau} = \tilde{\mathbb{C}} : \boldsymbol{\epsilon}^e = \det(\mathbf{I} + \boldsymbol{\epsilon}^e) \boldsymbol{\sigma} \quad (18)$$

Following similar procedure and consider Eqs. (7) – (12) (see [28] for more details), the kinematic equation and the elasticity equation are expressed in a simplified form. Box 1 summarizes the system of equations for the CPFE model with the small elastic strain assumption, together with the plasticity relationships, flow rule, evolution equations, Schmid's law and texture evolution equations discussed below.

<ul style="list-style-type: none"> • Equilibrium: $\operatorname{div} \boldsymbol{\sigma} = \mathbf{0}$ • Boundary conditions.: $\mathbf{u}(\mathbf{x}, t) = \bar{\mathbf{u}}(\mathbf{x}, t), \mathbf{x} \in \Gamma^u; \quad \boldsymbol{\sigma}(\mathbf{x}, t) \cdot \mathbf{n} = \bar{\mathbf{t}}(\mathbf{x}, t), \mathbf{x} \in \Gamma^t$ $\Gamma^u \cup \Gamma^t = \partial \mathbb{B}_0, \quad \Gamma^u \cap \Gamma^t = \emptyset$ • Kinematics: $\mathbf{W} = \tilde{\boldsymbol{\Omega}}^e + \tilde{\mathbf{W}}^p, \quad \tilde{\boldsymbol{\Omega}}^e = \dot{\mathbf{R}}^e \mathbf{R}^{eT}$ $\mathbf{D} = \tilde{\mathbf{D}}^p + \dot{\boldsymbol{\epsilon}}^e + \boldsymbol{\epsilon}^e \tilde{\boldsymbol{\Omega}}^e - \tilde{\boldsymbol{\Omega}}^e \boldsymbol{\epsilon}^e$ • Elasticity: $\boldsymbol{\tau} = \tilde{\mathbb{C}} : \boldsymbol{\epsilon}^e; \quad \boldsymbol{\tau} = \det(\mathbf{I} + \boldsymbol{\epsilon}^e) \boldsymbol{\sigma}$ • Plasticity: $\tilde{\mathbf{W}}^p = \mathbf{R}^e \bar{\mathbf{W}}^p \mathbf{R}^{eT} = \sum_{\alpha=1}^N \dot{\gamma}^\alpha (\tilde{\mathbf{Z}}^\alpha)_A$ $\tilde{\mathbf{D}}^p = \mathbf{R}^e \bar{\mathbf{D}}^p \mathbf{R}^{eT} = \sum_{\alpha=1}^N \dot{\gamma}^\alpha (\tilde{\mathbf{Z}}^\alpha)_S$ • Flow rule: $\dot{\gamma}^\alpha = \dot{\gamma}_0 \exp \left\{ - \frac{F_0}{k\theta} \left\langle 1 - \left\langle \frac{ \boldsymbol{\tau}^\alpha - B^\alpha - S^\alpha \mu / \mu_0}{\hat{\tau}_0 \mu / \mu_0} \right\rangle^p \right\rangle^q \right\} \operatorname{sgn}(\boldsymbol{\tau}^\alpha - B^\alpha)$ • Schmid's law: $\boldsymbol{\tau}^\alpha = \boldsymbol{\tau} : \tilde{\mathbf{Z}}^\alpha; \quad \tilde{\mathbf{Z}}^\alpha = \tilde{\mathbf{m}}^\alpha \otimes \tilde{\mathbf{n}}^\alpha$ • Texture evolution: $\tilde{\mathbf{m}} = \mathbf{R}^e \cdot \bar{\mathbf{m}}^\alpha; \quad \tilde{\mathbf{n}} = \mathbf{R}^e \cdot \bar{\mathbf{n}}^\alpha$ • Evolution equations: $\dot{S}^\alpha = [h_S - d_D(S^\alpha - \bar{S}^\alpha)] \dot{\gamma}^\alpha - h_2(S^\alpha - S_0^\alpha) H \left(\dot{\gamma}_{\text{th}} - \sum_{\alpha=1}^n \dot{\gamma}^\alpha \right)$ $\dot{B}^\alpha = [h_B - D^\alpha B^\alpha \operatorname{sgn}(\dot{\gamma}^\alpha)] \dot{\gamma}^\alpha$
--

Box 1: Summary of the CPFE model.

2.1 Flow rule and evolution equations

A number of flow rules have been used to model the kinematics of slip in alloys at high temperature [35, 6, 44, 25]. The one proposed by Busso to idealize the high temperature behavior of nickel-based alloys [6, 5, 24] is adopted in this study:

$$\dot{\gamma}^\alpha = \dot{\gamma}_0 \exp \left\{ -\frac{F_0}{k\theta} \left\langle 1 - \left\langle \frac{|\tau^\alpha - B^\alpha| - S^\alpha \mu / \mu_0}{\hat{\tau}_0 \mu / \mu_0} \right\rangle^p \right\rangle^q \right\} \operatorname{sgn}(\tau^\alpha - B^\alpha) \quad (19)$$

where, k is the Boltzmann constant, θ the temperature in Kelvin, $\dot{\gamma}_0$ the reference shear strain rate, F_0 the activation energy, $\hat{\tau}_0$ the stress at which dislocations can be mobilized without the assistance of thermal activation. p and q are two fitting parameters, μ and μ_0 the shear moduli at the current temperature and 0 K, respectively, S^α and B^α the slip resistance and backstress in the slip system α , respectively. $\langle \cdot \rangle$ denotes the Macaulay brackets (i.e., $\langle \cdot \rangle = ((\cdot) + |\cdot|)/2$), $\operatorname{sgn}(\cdot)$ is the sign function.

The starting point for the evolution equations for the slip resistance (S^α) and the backstress (B^α) for a nickel based alloy is [5, 24]:

$$\dot{S}^\alpha = [h_S - d_D(S^\alpha - S_0^\alpha)]|\dot{\gamma}^\alpha| \quad (20)$$

$$\dot{B}^\alpha = [h_B - D^\alpha B^\alpha \operatorname{sgn}(\dot{\gamma}^\alpha)]\dot{\gamma}^\alpha \quad (21)$$

where, S_0^α is the initial slip resistance for slip system α , h_S and d_D are the hardening and dynamic recovery parameters for the slip resistance evolution; h_B and D^α are the hardening and dynamic recovery parameters for the backstress evolution, and D^α is expressed as [24]:

$$D^\alpha = \frac{h_B \mu_0}{S^\alpha} \left\{ \frac{\mu'_0}{f} - \mu \right\}^{-1} \quad (22)$$

in which, μ'_0 is the local slip shear modulus at 0 K and f is a parameter that accounts for the coupling between the internal slip variables as well as the statistical effects.

The slip evolution laws described in Eqs. (20) and (21) have been used to describe the hardening behavior of nickel-based alloys at different temperatures (see [35, 6, 24]). **Fully reversed strain-controlled low cycle fatigue and creep-fatigue tests of IN 617 (with strain profile schematically illustrated in Fig. 2) were conducted at total strain ranges of 0.6–2.0% at 950°C.** A distinct pattern of stress-strain behavior is observed under

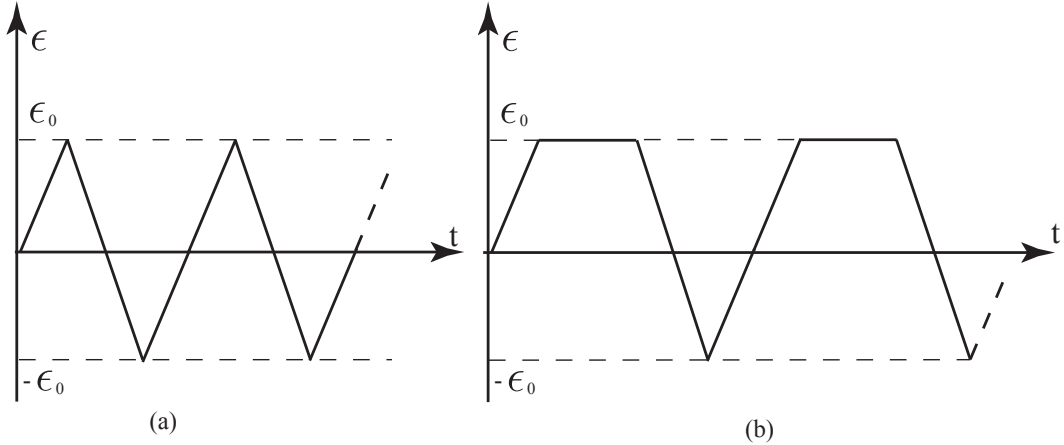


Figure 2: Strain profiles: (a) fatigue test; (b) creep-fatigue test

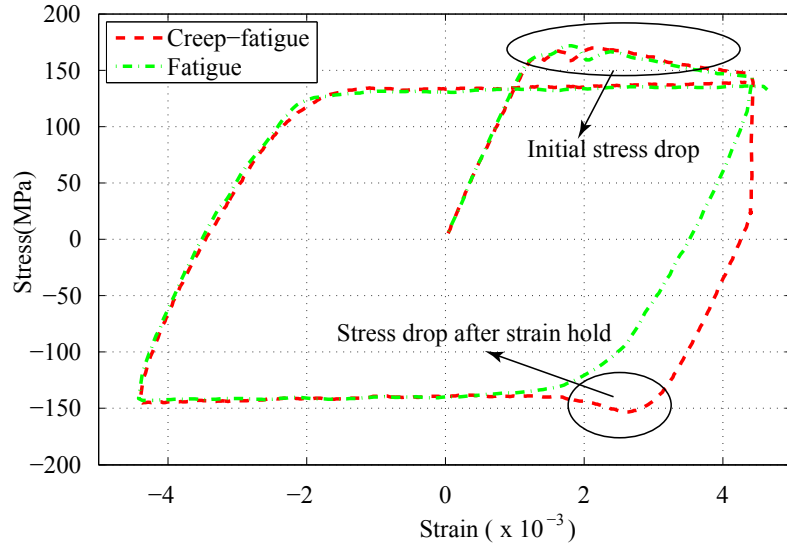


Figure 3: Stress drop observed in the stress-strain curve.

high-temperature fatigue and creep-fatigue loading (see Fig. 3), featured by: (1) an initial stress drop in the first cycle for both fatigue and creep-fatigue tests; (2) re-emergence of the softening behavior in creep-fatigue tests upon reloading (compression) following a strain hold, which is observed in all cycles until crack initiation. The evolution equations in Eqs. (20) and (21) do not capture this softening behavior.

The formation of an initial peak followed by an exponential decrease to a stable flow stress in IN 617 at high temperatures has been attributed to the solute-drag creep deformation mechanism [54]. Similar behavior has been observed in other alloys (e.g., class I and class A aluminum alloys) that exhibit solute-drag creep at elevated temperatures ([45, 47, 7]). Under pure fatigue, the phenomenon is restricted to the first cycle, whereas under creep-fatigue

loading, the transient softening prior to steady state flow is persistent.

While the mechanism of solute-drag creep is known [47], its recurrence under creep-fatigue loading has not been studied in detail to the best of the authors' knowledge. At elevated temperature and applied stress, the solutes hinder dislocation motion resulting in relatively high resistance to plastic flow. At a threshold stress, the dislocations overcome the energy barrier and begin dragging solute atoms, which consequently reduces the flow stress to a steady state. Under sudden load reversal, those solute atoms already dragged out of their equilibrium state do not contribute to the extra resistance observed in the initial loading. When subjected to a strain-hold with sufficiently long hold time, solutes return to an energetically minimum state. Hence, upon loading reversal, they contribute to added transient resistance to flow.

We model the above interactions by a new evolution law for the slip resistance given as:

$$\dot{S}^\alpha = [h_S - d_D(S^\alpha - \bar{S}^\alpha)]|\dot{\gamma}^\alpha| - h_2(S^\alpha - S_0^\alpha)H\left(\dot{\gamma}_{\text{th}} - \sum_{\alpha=1}^n |\dot{\gamma}^\alpha|\right) \quad (23)$$

where, $\dot{\gamma}_{\text{th}}$ is the threshold rate for static recovery, h_2 the rate of static recovery parameter, \bar{S}^α the steady state flow strength parameter. $H(\cdot)$ denotes the Heaviside function. The first part of the slip resistance evolution includes the steady state flow strength parameter, \bar{S}^α , which is typically lower than S_0^α - the “initial” slip resistance. **The initial slip resistance refers to the energetic configuration with stationary solutes prior to the onset of drag, and corresponds to the threshold stress mentioned above.** The second part of the slip resistance evolution accounts for the recovery of strain softening in the form of static recovery. In the present model, the recovery initiation is possible only when dislocation motion reduces significantly, which is a necessary condition to stop the drag process. Considering the Orowan equation:

$$\dot{\gamma}^\alpha = \rho_M^\alpha b v^\alpha \quad (24)$$

in which, v^α is the average velocity of the mobile dislocations, ρ_M^α the density of mobile dislocations and b the length of Burgers vector. We employ the proportionality between the diffusion velocity and the slip rate in Eq. (24) to define the recovery term. When magnitude of slip (at all slip systems) drops below a threshold rate, $\dot{\gamma}_{\text{th}}$, static recovery initiates. The rate of recovery is controlled by h_2 . At the asymptotic limit, the slip system strength reaches the initial slip system strength (i.e., configuration indistinguishable from the initial state).

The competition between the first and the second components of the strength

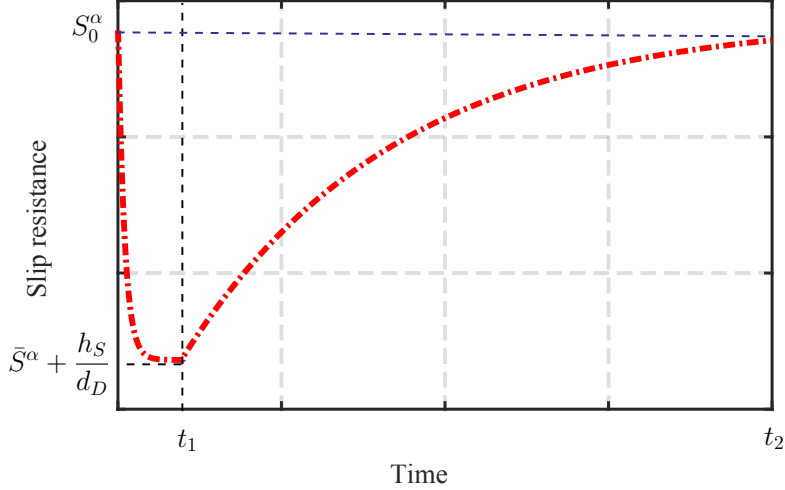


Figure 4: Evolution of slip resistance under the prescribed slip rate.

evolution equation, which respectively forces a reduction and increase in the slip resistance is explained in the context of a simple example. Consider an arbitrary slip system, α , is subjected to a constant slip rate $\dot{\gamma}^\alpha = \dot{\gamma} > \dot{\gamma}_{\text{th}}$ (with slip in all other slip systems constrained) until time t_1 , followed by zero slip rate $\dot{\gamma}^\alpha = 0$ between times t_1 and t_2 . The example is set to mimic loading followed by a subsequent strain hold. t_1 and t_2 are sufficiently long such that dynamic and static recovery processes are nearly completed, respectively. Under this prescribed loading condition, the evolution of slip resistance can be evaluated in closed form from Eq. (23) as:

$$S^\alpha = \begin{cases} \bar{S}^\alpha + \frac{1}{d_D} \left\{ h_S - [h_S - d_D(S_0^\alpha - \bar{S}^\alpha)] \exp(-d_D |\dot{\gamma}_0^\alpha| t) \right\} & 0 \leq t \leq t_1 \\ S_0^\alpha - (S_0^\alpha - \bar{S}^\alpha - \frac{h_S}{d_D}) \exp(-h_2(t - t_1)) & t_1 \leq t \leq t_2 \end{cases} \quad (25)$$

Equation (25) plotted in Fig. 4 shows an exponential decay of the slip resistance towards $\bar{S}^\alpha + h_S/dD$ followed by a recovery towards its initial value S_0^α .

2.2 Numerical smoothing for convergent stress update

Box 1 summarizes the system of nonlinear equations, which describes the mechanical response based on the crystal plasticity model described above. This system is discretized over the domain of a characteristic microstructure and evaluated numerically using the finite element method. The stress update at a material point within a grain is performed using an operator split method with a two-level staggering scheme as described in Refs. [27, 28]. In the first level,

a Newton-Raphson method is used to solve for stress ($\boldsymbol{\tau}$), while rotations (\boldsymbol{R}^e), slip resistances (S^α) and backstress (B^α) are kept constant; In the second level, rotations, slip resistances and backstress are updated for a fixed stress calculated at the first level. Iterations between the two levels continue until changes in the cardinal unknowns (i.e., $\boldsymbol{\tau}$, S^α and B^α) within the increment drop below a threshold value (relative change of the norm is less than 1.0×10^{-4} in the current study). Convergence of the polycrystal plasticity equations summarized in Box 1 using the algorithms defined above is not guaranteed due to the discontinuity in the Jacobian introduced by the presence of Macaulay brackets in the flow rule. This discontinuity typically leads to the oscillation of the iterations without convergence. We employ a simple regularization of this problem, by replacing the Macaulay brackets with a C^1 continuous approximation. Let $\langle f \rangle_c$ be a C^1 continuous functional defined as (Fig. 5):

$$\langle f \rangle_c = \begin{cases} f & f > \frac{1}{\sqrt{2}}c \\ r - \sqrt{r^2 - f^2 + 2fc} & -c \leq f \leq \frac{1}{\sqrt{2}}c \\ 0 & f < -c \end{cases} \quad (26)$$

where, $r = (\tan \frac{3\pi}{8})c$ is the radius of the circle that is used for smoothing. At the limit of $c \rightarrow 0$, $\langle f \rangle_c$ approaches $\langle f \rangle$ and c constitutes the numerical regularization parameter. The Macaulay bracket in the slip evolution equation is then replaced with the continuous approximation. In the numerical simulations discussed below c is set to 0.001. By this approach, the system Jacobian remains well-defined and the numerical scheme is convergent for sufficiently small time step size. We note that the convergence is sub-quadratic due to the use of operator split in the evolution of the constitutive equations.

3 Model preparation

IN 617 is a solid solution strengthened alloy with face center cubic (FCC) lattice structure, with 12 octahedral $\{100\}\langle 110 \rangle$ slip systems. In precipitate strengthened nickel alloys where the $\gamma-\gamma'$ phases coexist, the six cubic slip systems $\{100\}\langle 110 \rangle$ may also contribute to deformation at high homologous temperatures and high resolved stress (in γ' phase) [44]. γ' phase becomes unstable above 650°C [26, 4]. At temperatures above approximately 750 °C, the microstructure of IN 617 is largely free of γ' precipitates, hence the cubic slip systems remain inactive. Figure

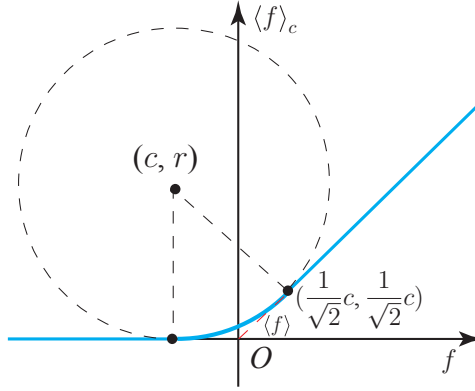


Figure 5: “Smoothed” Macaulay bracket to eliminate Jacobian discontinuity and improve stress-update convergence.

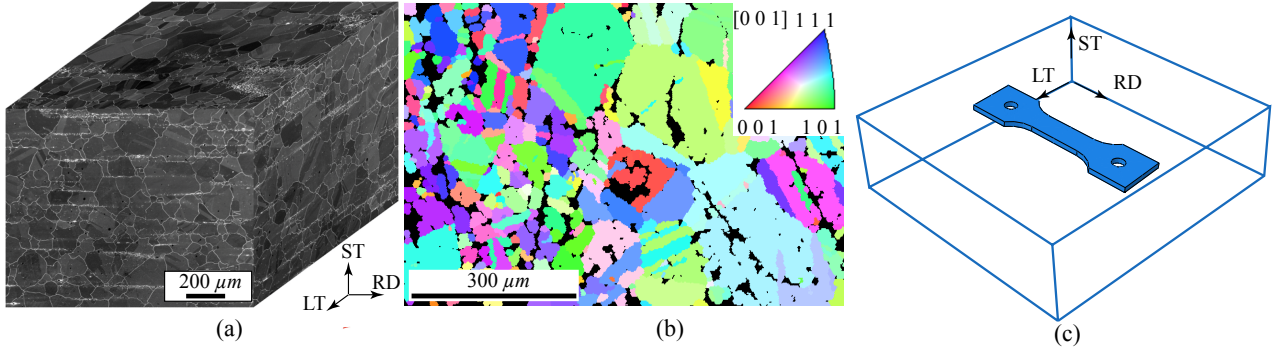


Figure 6: IN 617 microstructure: (a) 3-D etched microstructure (reproduced from Ref. [30]; (b) **[0 0 1] inverse pole figure (IPF) EBSD map on a short traverse plane of as received IN 617 sample;** (c) specimen configuration.

6(b) shows a 2-D EBSD scan of IN 617. The microstructure exhibits distinguishable coarse and fine grains and random initial orientations as shown in Fig. 6(b). Similar observations have been previously made [30, 31, 29]. Annealing twins are evident in the as-received samples and deformation twinning has not been observed and not considered in the simulations. **Annealing twins could serve as sites of strain localization and damage initiation in Ni-based alloys subjected to fatigue loading conditions [59, 60]. The focus of the current investigations is on modeling of the cyclic response prior to the onset of significant microstructural damage, and the presence of annealing twins are not taken into account in the microstructures employed in this study.** The microstructure images (Fig. 6(a)) also show significant amount of carbides (mainly Mo-rich, Cr-rich carbides and Ti-rich carbonitrides) present within and at grain boundaries. While the presence of carbides may affect the fatigue and creep-fatigue damage, they are not explicitly modeled in the simulation of the cyclic behavior.

Table 2: Summary of all tests studied.

Specimen	Temperature(°C)	Strain rate (/s)	Total Strain (%)	Hold time (s)
B-14	950	0.001	0.6	0
E-11	950	0.001	1.0	0
J-1	950	0.001	2.0	0
A-14	950	0.001	0.6	600
416-18	950	0.001	0.6	1800
B-16	950	0.001	0.6	180
F-5	950	0.001	1.0	180
A-13	950	0.001	1.0	600
E-6	950	0.001	1.0	1800
E-10	950	0.001	1.0	9000

All experimental data used in this study are from specimens machined from the annealed plate produced by ThyssenKrupp VDM and solution annealed at 1175 °C [55]. The compositions of the specimens are given in Table 1 along with the specified ranges in ASTM Standard B168-08 for comparison. **The long axis of the specimen is aligned with the rolling direction as schematically demonstrated in Fig. 6(c).**

Table 1: Composition in percentage weight of the IN 617 specimen used in this study.

	Ni	C	Cr	Co	Mo	Fe
ASTM standard	≥ 44.5	0.05-0.15	20.0-24.0	10.0-15.0	8.0-10.0	≤ 3.0
This study	bal	0.05	22.2	11.6	8.6	1.6
	Al	Ti	Si	Cu	Mn	S
ASTM standard	0.8-1.5	≤ 0.6	≤ 1.0	≤ 0.5	≤ 1.0	≤ 0.015
This study	1.1	0.4	0.1	0.04	0.1	≤ 0.02

Fully reversed strain-controlled low cycle fatigue and creep-fatigue tests were conducted at total strain ranges from 0.6-2.0% at 950°C, all with constant strain rate of 1.0×10^{-3} /s. One cycle was defined as the combination of a tension and compression load reversal using a symmetric triangular waveform. During the initial part of most experiments, several cycles with incrementally increasing strain values were used prior to reaching the target strain level to avoid overshooting the target strain, which can occur at high temperature in the presence of plastic deformation. Table 2 summarizes the experiments used in this study.

3.1 Microstructure reconstruction and meshing

Microstructure generation of IN 617 is conducted using the DREAM.3D software [17], which is capable of creating synthetic microstructures using experimentally determined microstruc-

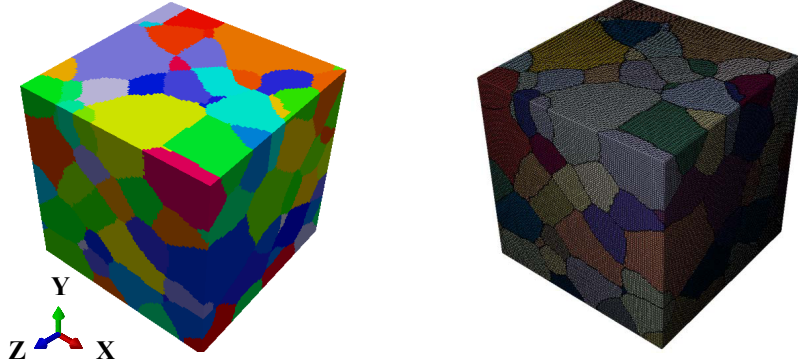


Figure 7: Mistructure genertion and meshing: (a) microstructure generated in DREAM.3D; (b) volume mesh.

ture morphological and crystallographic statistics. Grain size distribution computed from microstructure observations are employed to generate the synthetic microstructures, as well as their geometry and surface mesh information (see Fig. 7(a)). To accurately quantify the bi-modal grain size distribution observed in IN 617, the fine and coarse grains are treated as separate phases during the reconstruction process. The volume fractions of the fine and coarse grains are 75.61% and 24.39%, respectively. Figure 8 shows the log-normal distributions fitted to the experimentally observed distributions for both the fine and coarse grains. The Parallelized Polycrystal Mesher (PPM) software developed by Cerrone et al [11] is then used to build a volume mesh of the microstructures. Figure 7(b) shows the volume mesh generated using the above-mentioned process, **which provides statically equivalent microstructures as the specimen.**

3.2 Determination of the simulation domain size

In order to identify the appropriate size of the simulation domain that provides converged CPFE simulation results with reasonable computational cost, a parametric study was conducted. The parametric study was performed with respect to the number of grains resolved within the simulated microstructure. Three different cubic simulation cells with edge length of 300 μm , 360 μm and 400 μm are constructed for this purpose. The discretization of the simulation cells are as shown in Fig. 9(b)-(d). The boundary conditions are schematically shown in Fig. 9(a). The three simulation cells contain 98, 140 and 243 grains, and are discretized using four-noded tetrahedra with 67,689, 113,986 and 243,801 elements, respectively. Each grain is assigned a random initial orientation. The applied strain follows a creep-fatigue test path with

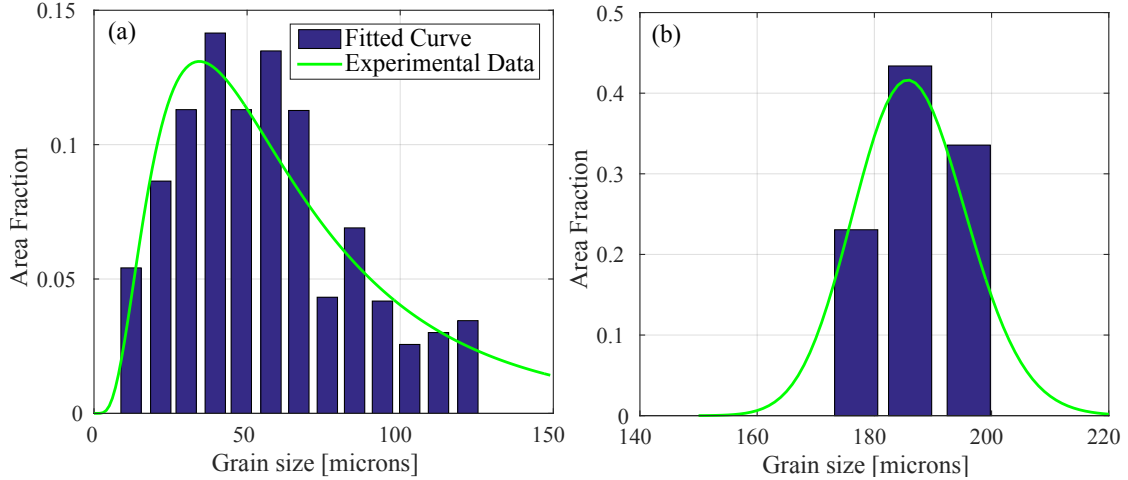


Figure 8: Fitted log-normal grain size distribution: (a) fine grains; (b) coarse grains.

1.0% strain range (R ratio equals to 1), 180 s hold time at the maximum tension and strain rate of 0.001/s.

Figure 10 shows the stress-strain responses obtained using the three simulation cells. While the three curves matched well during the elastic region and the stress hold, a noticeable gap between the 98-grain cell and the others is observed after yielding. This observation indicates 98-grain cell is not representative of a converged response while the simulation cell with 140 and 243 grains are sufficiently similar. **We further investigate the convergence of the local stress distribution within five microstructures, including a 504- and 769-grain cells (microstructure geometries not plotted for brevity).** The stress histograms of the cells at the beginning of the strain hold are plotted in Fig. 11. With the exception of the 98-grain cell, the stress distributions with the remainder of the cells are similar with slight variability. The CPFE simulations below are therefore performed using the 140-grain cell. The simulation cell is assigned with random initial texture with the $\{111\}$ pole figure shown in Fig. 12.

3.3 Model parameter calibration

The full set of parameter values of the crystal plasticity model for IN 617 described above is not generally available in the literature. Those model parameters not available in the literature are therefore inferred from experimental data. The general calibration approach used in this study is based on optimization through the minimization of an objective function. Let Θ denote the set of all unknown parameters of the model. In the current study, 19 parameters

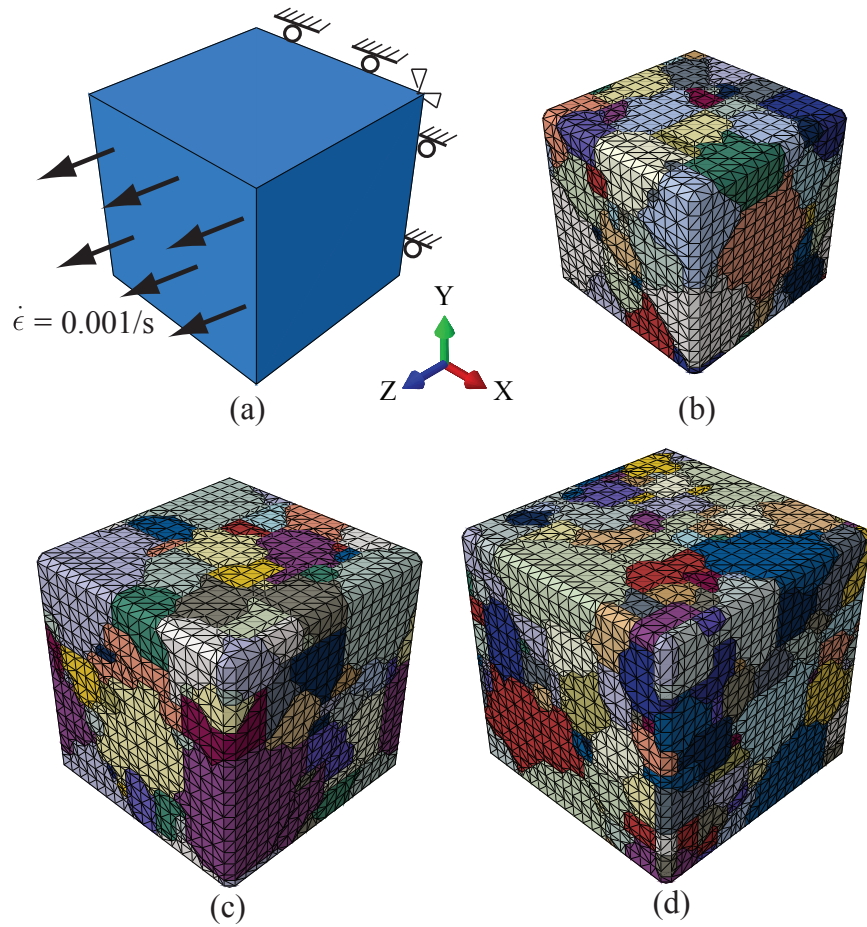


Figure 9: (a) Schematic illustration of the boundary conditions and loading used in the microstructure size determination study; (b)-(d) Finite element meshes of the 98-, 140- and 243-grain microstructures.

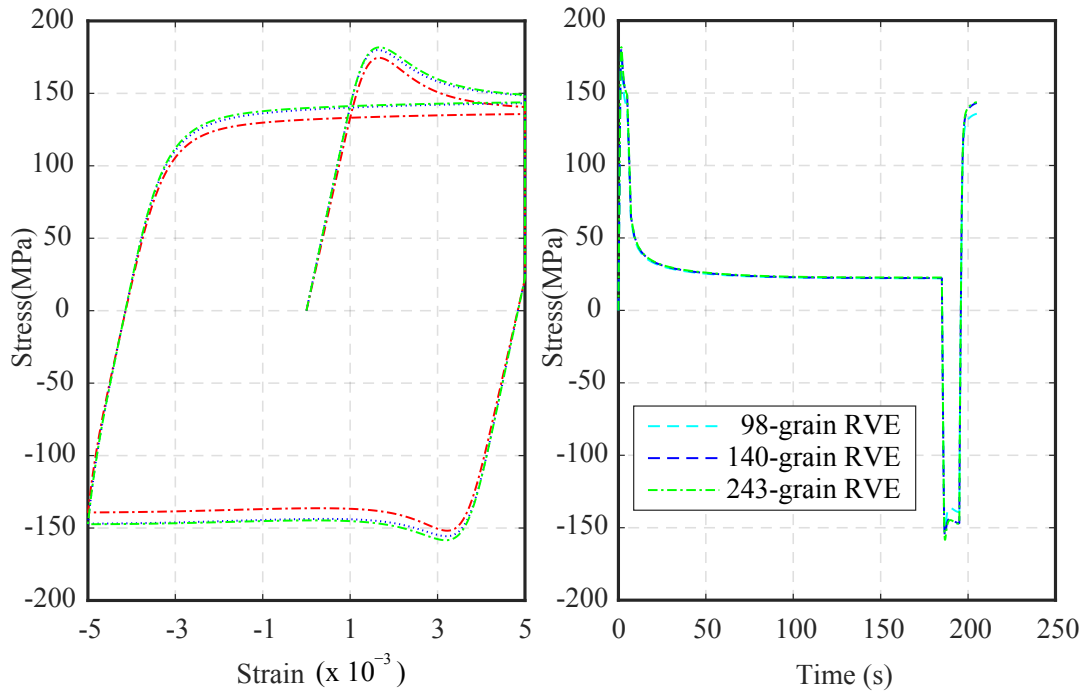


Figure 10: Convergence study of microstructure size: (a) stress-strain response; (b) stress-time response.

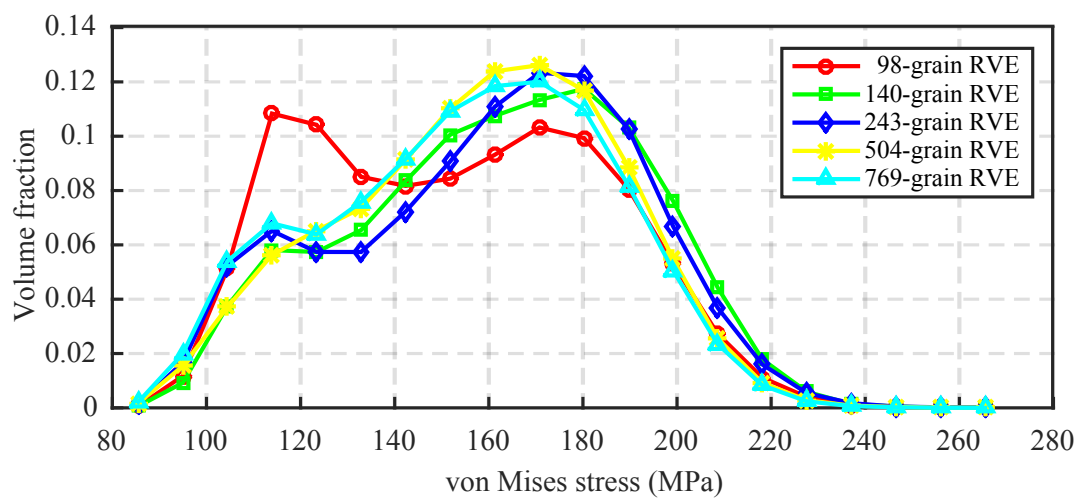


Figure 11: von-Mises stress histogram of different RVEs.

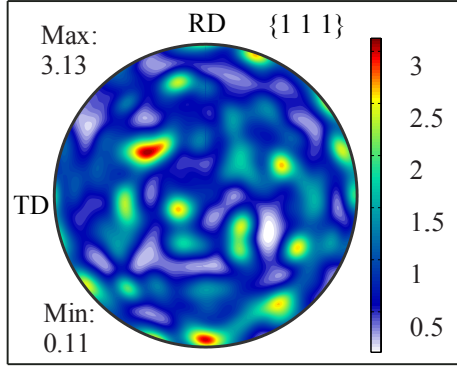


Figure 12: $\{1\ 1\ 1\}$ pole figure of the initial texture of the 140-grain microstructure.

define the model as indicated in Table 3. Consider an arbitrary but fixed subset of model parameters, $\hat{\Theta} \subset \Theta$. Each parameter within the parameter set, $\Theta_i \in \Theta$, lies within a range of values $\Theta_i \in [\Theta_i^l, \Theta_i^u]$, where Θ_i^l and Θ_i^u denote the lower and upper bound values of the parameter Θ_i , respectively. These bounds are typically chosen based on physical arguments, (e.g., magnitude of relative yield stress or strain hardening). The optimal set of parameters is achieved by solving the following equation:

$$\hat{\Theta}^{\text{opt}} = \arg \min \left\{ \sum_{i=1}^M w_i^t \left[\sum_{j=1}^{N_i} \left(\frac{R_{i,j}^{\text{exp}} - R_{i,j}^{\text{sim}}(\mathbf{X}_k)}{R_{i,j}^{\text{exp}}} \right)^2 \right], \hat{\Theta} \in [\hat{\Theta}^l, \hat{\Theta}^u] \right\} \quad (27)$$

in which, M is the total number of experiments used in the calibration process; w_i^t is the weight factor for the i^{th} test used to increase or reduce parameter sensitivity; N_i denotes the number of datasets obtained from test i (e.g., stress-strain, stress time histories); $R_{i,j}^{\text{exp}}$ and $R_{i,j}^{\text{sim}}$ are respectively the experimental and the simulated datasets. Equation (27) is written for a subset of parameters only and executed multiple times to calibrate all parameters, since the optimization of the full set of 19 parameters together is computationally prohibitive. At the beginning of the calibration process, each parameter is assigned an initial value, Θ_i^0 . During the calibration of the parameter subset $\hat{\Theta}$, all parameters (not being calibrated) are either set to their initial values, or set to their calibrated values at an earlier parameter subset calibration. We further note that a very comprehensive dataset is necessary to uniquely identify all parameters, and experimental data is often quite limited. We therefore seek a set of optimal and physically reasonable parameters that accurately captures the available calibration data. The calibration is performed by executing the following steps: (1) Determine search range for each parameter (i.e., Θ_i^l and Θ_i^u). (2) Sample parameter subspace and execute CPFE

simulations to compute $R_{i,j}^{sim}$. (3) Fit a surrogate model that approximates the response surface (i.e., $R_{i,j}^{sim}$). (4) Solve Eq. (27) to obtain optimal parameters set $\hat{\Theta}^{\text{opt}}$. (5) Verify calibration accuracy by running CPFE simulation with $\hat{\Theta}^{\text{opt}}$.

Two out of the 19 parameters are set to fixed values and not calibrated, while three of them are dependent (i.e., can be computed from the remaining 16). The optimizations are therefore performed for 14 parameters only. f is set to 0.36 as suggested by Lin et al. [24] since its effect on the simulation results are found to be small. The lattice friction stress at 0 K, $\hat{\tau}_0$, in Eq. (19) is obtained by resolving the difference between the yield strength (at 0.2% offset strain) at 0 K, $\sigma_{0.2}^0$, and the temperature approaching infinity, $\sigma_{0.2}^\infty$ (i.e., see [6]):

$$\hat{\tau}_0 = \frac{\sigma_{0.2}^0 - \sigma_{0.2}^\infty}{2} \quad (28)$$

with $\sigma_{0.2}^0$ and $\sigma_{0.2}^\infty$ estimated from Ref. [20], giving $\hat{\tau}_0 = 268.2$ MPa as a constant. This procedure has been previously employed to calibrate lattice friction stress [6]. A fixed anisotropy factor of $A = 2C_{44}/(C_{11} - C_{12}) = 2.5$ which is equal to that of pure nickel is enforced [36], decreasing the number of independent elastic parameters to two. The local shear modulus at 0 K, μ'_0 , is given by Ref. [6] as:

$$\mu'_0 = \frac{C_{11} - C_{12}}{2} \quad (29)$$

and the shear modulus μ is equal to the elastic parameter C_{44} .

The search ranges for the remaining 14 parameters of the polycrystal model are established through the literature search on crystal plasticity modeling of similar alloys, and preliminary parametric analysis performed for each parameter. The elastic properties for pure nickel are used as the initial value of the elastic parameter (i.e., $C_{11} = 250$ GPa, $C_{12} = 151$ GPa, $C_{44} = 123$ GPa [36]). By referring to elastic parameters of other nickel-based alloys [44, 24] and the observation that bulk moduli of alloy at 950°C is around 140 GPa, the ranges of C_{11} and C_{12} are set to be $150 \leq C_{11} \leq 280$ GPa and $30 \leq C_{12} \leq 160$ GPa, respectively. The activation energy F_0 for various nickel-based alloys was taken to be around 300 KJ/mol (4.98×10^{-19} J) in Refs. [44, 24, 5], which serves as the initial value of F_0 with the range set to be $4.5 \times 10^{-19} \leq F_0 \leq 5.5 \times 10^{-19}$ J. The initial values for p and q are chosen to be $p = 0.31, q = 1.8$ [24] with recommendation as $0 \leq p \leq 1$ and $1 \leq q \leq 2$ in general by Kothari and Anand [22], while preliminary simulations further constrain them as $0.1 \leq p \leq 0.4$ and $1.5 \leq q \leq 2$. The initial values and ranges of the other parameters are provided in Table 3.

Table 3: Summary of model parameters. (For fixed parameters, only initial value are provided; for dependent parameters, only dependency and calibrated value are provided.)

Parameter	Initial value	Lower bound	Upper bound	Calibrated value	Reference
C_{11} (GPa)	250	150	280	170.64	[36, 44, 24]
C_{12} (GPa)	151	30	160	108.39	[36, 44, 24]
$\dot{\gamma}_0$ (s^{-1})	5×10^{-3}	5×10^{-4}	3×10^{-2}	1.44×10^{-3}	[24]
F_0 (J)	4.98×10^{-19}	4.5×10^{-19}	5.5×10^{-19}	5.148×10^{-19}	[24, 44, 5]
μ_0 (GPa)	200	180	300	265.33	[24, 44, 5]
p	0.3	0.1	0.4	0.181	[22, 24]
q	1.8	1.5	2	1.633	[22, 24]
h_S (MPa)	2000	100	10000	397.73	[24, 5]
d_D (MPa)	100	1000	10000	5073.62	[24, 5]
S_0^α (MPa)	200	50	320	143.41	[24, 5]
\bar{S}^α (MPa)	200	20	S_0^α	18.03	-
h_B (MPa)	5000	10	10000	104.31	[24]
h_2 (MPa)	0	0	0.2	0.015	-
$\dot{\gamma}_{th}$ (s^{-1})	0	0	1×10^{-4}	1×10^{-6}	-
C_{44} (MPa)	$1.25(C_{11} - C_{12})$	-	-	77.82	[36]
μ (GPa)	$1.25(C_{11} - C_{12})$	-	-	77.82	[6]
μ'_0 (GPa)	$0.5(C_{11} - C_{12})$	-	-	31.13	[6]
$\hat{\tau}_0$ (MPa)	268.2	-	-	-	[6, 20]
f	0.36	-	-	-	[24]

The initial values used to initiate the optimization process that provided the global minimum are reported in the table.

Since the computational cost of CPFE simulations is high, it is computationally too costly to evaluate the minimization process using CPFE analysis as the forward solver. We rely on a surrogate model (i.e., Gaussian Process model [39]) to approximate the CPFE simulation for calibration purposes. GP model is a variant of a radial basis function built on Gaussian kernels and provides the fast transform function between the input (parameter set) and output ($R_{i,j}^{\text{sim}}$). The GP model is “trained” using a series of simulations using the CPFE. We employed Latin Hypercube sampling to sample the search space bounded by the parameter ranges. The optimization is performed using a constrained nonlinear multi-variable solver [37], where the objective function evaluations are performed using the GP models [68]. **In order to ensure that the global minimum is achieved within the chosen parameter ranges, The optimization process is repeated several times with random initial parameter values.** The final step consists of running a CPFE simulation, with optimal parameter set to assess accuracy. If accuracy is deemed insufficient, the GP model is retrained with denser

sampling around the optimal point within the parameter space. The optimization procedure is repeated with retrained GP model.

In this study, the calibration is performed for elastic, monotonic and cyclic response in order to limit the number of unknowns (i.e., dimension of parameter space). Since the fatigue and creep-fatigue tests provide the same response of the elastic and monotonic case, only one test (F-5) is used for calibration while a fatigue and creep-fatigue (F-5 and J-1) are used during the cyclic calibration process. In the elastic calibration process, bulk Young's modulus is taken to be $E = 141$ GPa according to the experimental data while Poisson's ratio of the bulk material is reported to be 0.3 at 950°C. The number of variables to be calibrated is equal to the number of properties, leading elastic calibration to a well-posed and unique optimization problem. (i.e., $\mathbf{X}_1 = \{C_{11}, C_{12}\}$, $\mathbf{R}_1 = \{E, \nu\}$).

In the monotonic calibration process, the softening part of the stress-strain curves are not considered at first while the slip resistance and backstress evolution are turned off (i.e., set initial value temporarily as: $h_S = 0, d_D = 0, h_B = 0, h_2 = 0$) in the simulation. $R_{1,j}$ is the j^{th} data point out of the total N_1 data points selected from the tension part of the stress-strain curve with the stress drop region eliminated, while $\mathbf{X}_2 = \{F_0, S_0^\alpha, \mu_0\}$ and $\mathbf{X}_3 = \{S_0^\alpha, \dot{\gamma}_0, p, q\}$ are calibrated successively. Then another set of selected data points from the tension part of the stress-strain curve that mainly characterizes the initial yield stress, the stress drop speed and the stabilized flow stress are used in the objective function while the parameters set is chosen as $\mathbf{X}_4 = \{\bar{S}^\alpha, h_S, d_D, h_B\}$ with the static recovery term turned off (i.e., set initial value temporarily as: $h_2 = 0$).

In the cyclic calibration process, both fatigue test J-1 and creep-fatigue test F-5 are used to define the objective function. Data points that reflect the relaxation, yielding stress at compression, softening after the strain hold in the creep-fatigue test and hardening profile are selected while $\mathbf{X}_5 = \{p, q, \dot{\gamma}_0, h_2, \dot{\gamma}_{th}\}$ are used to match hysteresis response for both the fatigue and creep-fatigue tests. The final calibrated parameters are listed in Table 3, while the simulation results together with corresponding experimental tests are plotted in Fig. 13. It can be seen that the calibrated parameters can capture the stress-strain and stress-time response for both fatigue test and creep-fatigue tests with good accuracy. Their capability to predict other fatigue and creep-fatigue tests with different strain ranges and hold times is further validated next.

The primary challenges in the proposed optimization strategy, particularly for

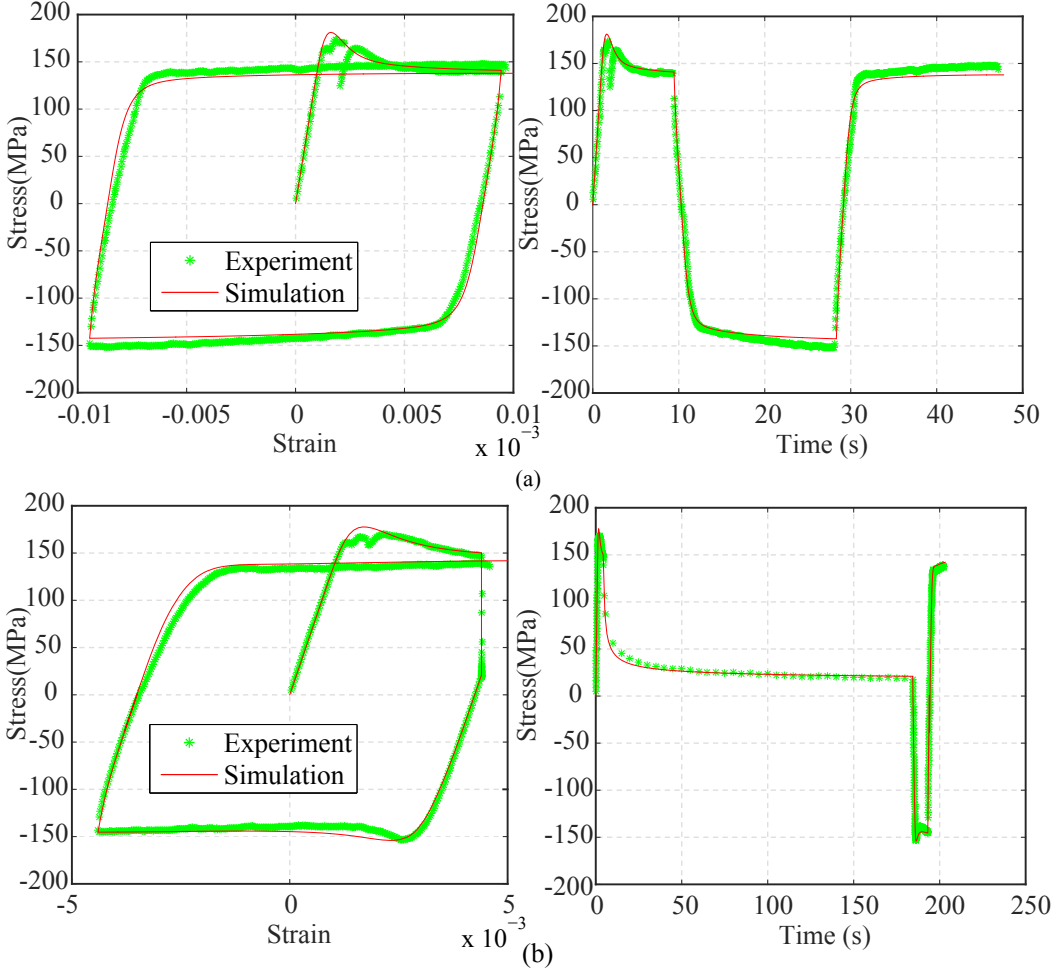


Figure 13: Comparison of simulation results using the calibrated parameters with the two experiment tests used for calibration: (a) fatigue test J-1; (b) creep-fatigue test F-5.

generalizing beyond the current study, are the identification of the parameter ranges and parameter sensitivity used in the selection of parameter subsets. The sensitivity analysis, which identifies the parameters with similar sensitivity (i.e., the selected parameter subset) to the corresponding experimental data used to calibrate them, depends on the chosen parameter ranges. In the current study the parameter ranges were identified based on a parametric study and values previously reported in the literature as discussed above. These challenges exist because of the relatively large number of parameters to be identified, and because the experiments are performed at the bulk scale to calibrate parameters defined at the grain scale.

4 Validation and analysis of microstructural response

The calibrated parameters are further validated by running CPFE simulations to compare the first cycle response with experimental data of the remaining tests. As illustrated in Table 2, the tests were performed using various strain ranges and hold times beyond the calibration regime. The comparisons are first focused on the first cycle response. A multiple-cycle analysis and discussion is presented next.

4.1 First cycle response

Since the transient stress relaxation phenomenon is most prominent in the first cycle, particularly when subjected to fatigue loading, we first investigate the predictive capability of the proposed model in capturing the hysteresis behavior of the first cycle. In this section, we also provide a brief analysis of the evolution of the hysteresis behavior through the cycles and an investigation of the evolution of the stress state within the microstructure.

Figure 14 shows the first cycle responses of fatigue tests B-14 and E-11, respectively. The creep-fatigue tests B-16, A-14 and A-13 are shown in Fig. 15 while creep-fatigue tests 416-18, E-6 and E-10 are shown in Fig. 16. The applied strain ranges in B-16, A-14 and 416-18 are small enough such that the stress softening behavior is not significant. The stress softening effect is visible and prominent beyond approximately 0.3% and appears in the other fatigue and creep-fatigue tests. The initial tensile loading part of the stress-strain curves in all experiments is also marked by the presence of serrations induced by the Portevin-Le Chatelier effect [54]. The present approach does not account for this effect and the tensile loading part of the simulations exhibit a smooth loading path.

In view of the above-mentioned points, the simulated overall stress-strain hysteresis curves are in very good agreement with the experiments. In particular, the stress relaxations caused by solute-drag creep are accurately captured as a function of various hold times and strain ranges. Particularly, Fig. 16 reveals slight discrepancies in the experimentally observed and simulated compressive flow stresses for creep fatigue tests E-6 and E-10, where the simulations overestimate the flow stress especially during the transient relaxation part. Nevertheless, comparing to the remainder of the creep-fatigue experiments, the simulation results remain within experimental error range.

The evolution of the hysteresis behavior as a function of load cycles are analyzed in the

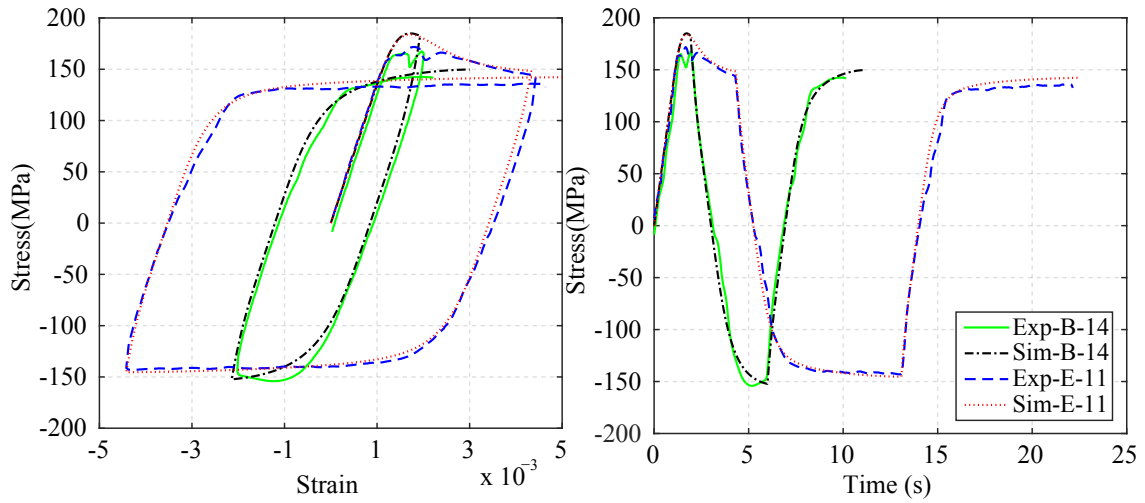


Figure 14: First cycle response of fatigue test B-14 and E-11.

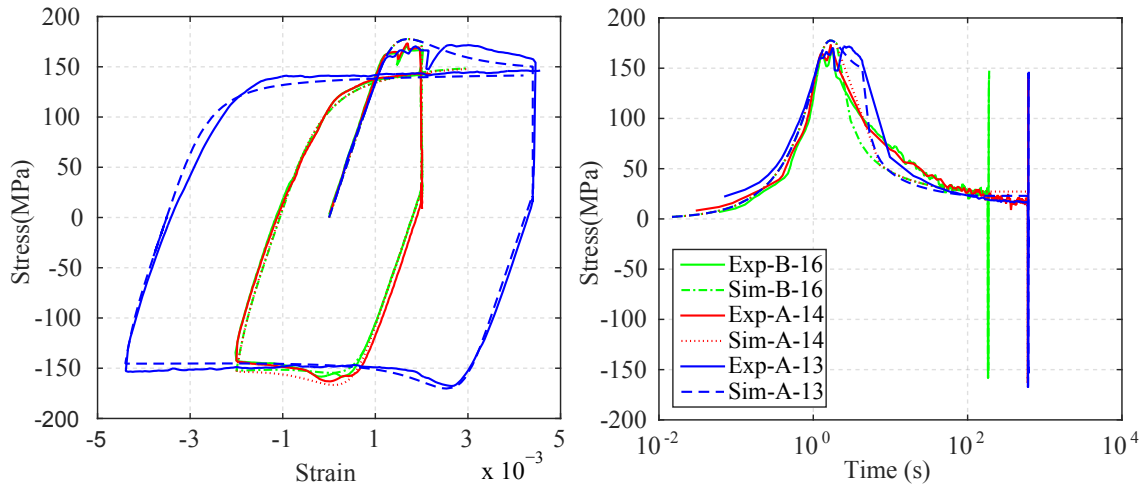


Figure 15: First cycle response of creep-fatigue test B-16, A-14 and A-13.

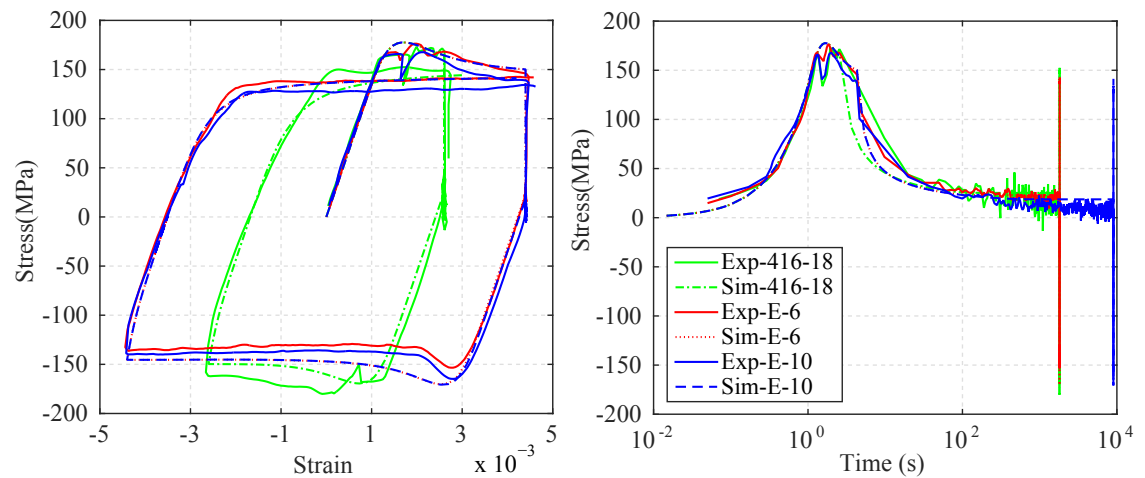


Figure 16: First cycle response of creep-fatigue test 416-18, E-6 and E-10.

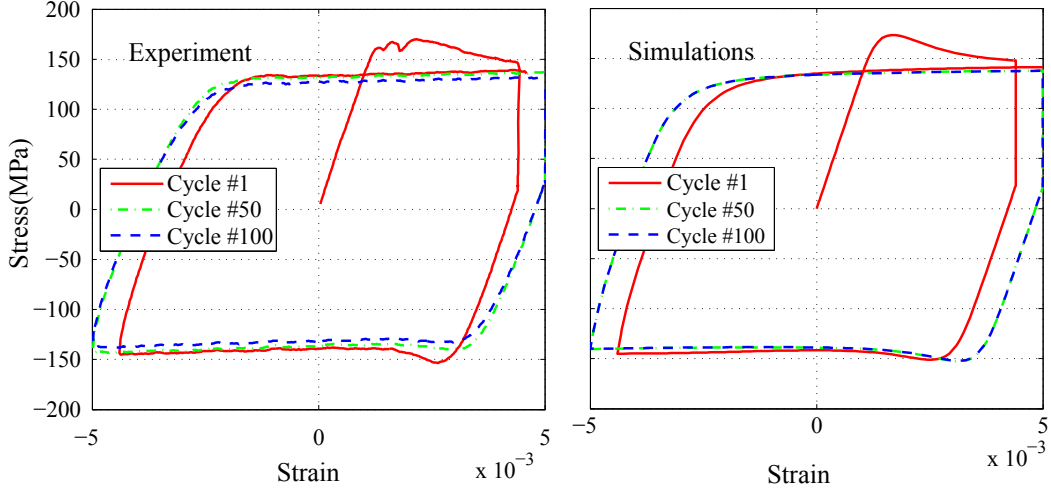


Figure 17: Stress-strain curves of different cycles: (a) experiments; (b) simulations.

context of experiment F-5, which is a creep-fatigue experiment with applied total strain range of 1% and hold time of 180 s. Figure 17 shows the hysteresis loops of the 1st, 50th and 100th cycles from both the experiments and the simulations. The experimentally observed creep-fatigue life of the specimens is 465 cycles. The deformation therefore remains within the viscoplastic regime, with only a small effect of creep processes within the first 100 cycles. The experiment hysteresis loops demonstrate a slightly larger amount of cyclic softening, compared to the simulations. We note that a small amount of cyclic softening is also observed in simulation results due to the viscoplastic processes modeled in the context of grain deformation. The slight discrepancy between the experimental and simulated cyclic softening is due to the presence of (albeit small) diffusional grain boundary damage (e.g., cavitation) present in the experiments. The current model does not account for creep or fatigue induced damage evolution and these important effects will be investigated in the near future.

4.2 Microstructure analysis

The stress distributions within the simulation cell are investigated to gain more understanding of the microstructural aspects of deformation. The analyses are based on the creep-fatigue experiment, F-5. Figure 18 shows the stress contour plots over the simulation cell at the beginning, middle and end of hold of the first loading cycle. A complex stress distribution over the microstructure domain is observed with significant stress variations within and between grains, due to differences in grain orientations within the microstructure [14]. Stress

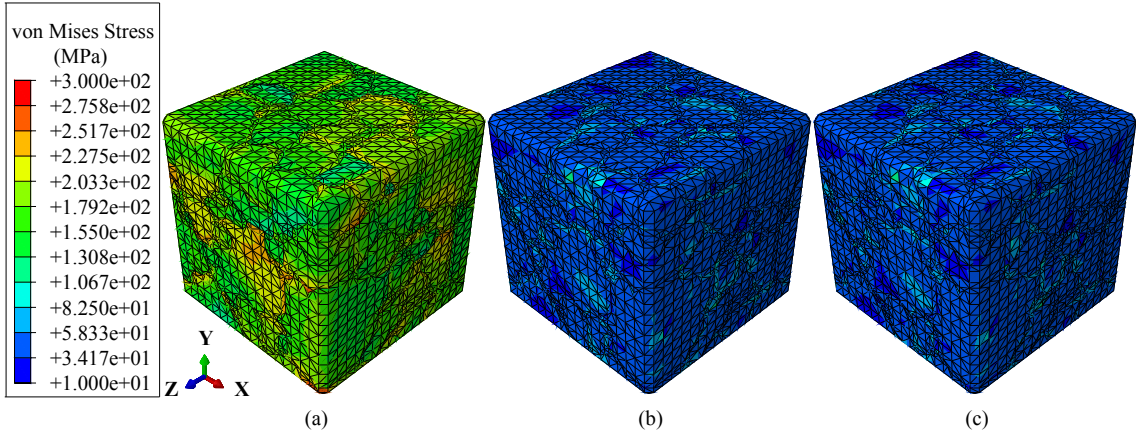


Figure 18: Stress contour of the RVE of the first cycle: (a) beginning of hold; (b) middle of hold; (c) end of hold.

Table 4: Orientations (Bunge's convention) and misorientations of adjacent grains at the high stress locations.

Orientations of grain A	Orientations of Grain B	Misorientation
(148.51, 61.1, 291.5)	(352.38, 144.74, 242.35)	38.24
(279.2, 44.29, 98.96)	(311.07, 97.24, 264.9)	45.85
(250.05, 44.24, 131.00)	(237.19, 115.02, 41.72)	51.61
(237.19, 115.02, 41.72)	(67.62, 65.15, 257.39)	34.79
(32.61, 48.65, 182.49)	(354.55, 84.24, 67.38)	57.48
(149.75, 133.74, 160.51)	(207.01, 153.38, 27.1)	37.54

concentrations around grain boundaries are also observed, with a naturally higher tendency of stress concentrations with higher misorientation angles. **The locations of high stress concentrations (von-Mises stress higher than a threshold magnitude of 280 MPa) are highlighted in Fig. 19. It is observed that all of these locations are at the grain boundaries, and the orientations and misorientations around the locations of high stress are shown in Table 4. The misorientation angles are computed using the following equation [61, 14]:**

$$\theta = \min \left| \cos^{-1} \left\{ \frac{\text{tr}(\mathbf{g}_B \mathbf{g}_A^{-1} \mathbf{O}) - 1}{2} \right\} \right| \quad (30)$$

where, \mathbf{g}_A and \mathbf{g}_B are the orientation matrices of adjacent grains A and B , respectively, tr is the trace operator, and \mathbf{O} is the crystal symmetry operator for FCC crystals.

The stress contours also indicate only a small amount stress redistribution occurs at the

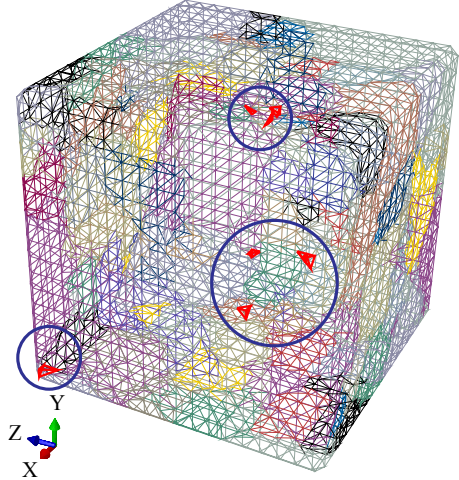


Figure 19: Locations with von-Mises Stress higher than 280 MPa at the beginning of hold.

latter half of the hold (compare Figs. 18(b) and (c)) since the stress relaxation process has largely been completed within the first half of the strain hold. The significant stress relaxation observed during the first part of the hold is also associated with a stress redistribution. The effect of stress redistribution is further demonstrated using the von-Mises stress histograms as shown in Fig. 20 for the first, 50th and 100th cycles. The slight leftward shift of the mean stress at the beginning of strain hold from the first to the 100th cycle indicates the viscoplastic cyclic softening process. The $\{111\}$ pole figure of the microstructure at different stages of the hold (from the first loading cycle) shown in Fig. 21 indicates no obvious texture evolution within the cycle. The subsequent loading cycles also did not indicate significant texture evolution.

To further investigate the distribution of stresses within and across grains, stress is plotted along the center line of the simulation cell along the X -direction as shown in Fig. 22. The dashed vertical lines indicate the grain boundaries, while each little cube shows the initial orientation of each grain relative to the sample coordinate system (Fig. 22(a)). Depending on the orientation of a grain with respect to the loading axis, those exhibit large plastic deformations are denoted as soft grains, and those have little or no plasticity are denoted as hard grains. Hard and soft grains are clearly recognized by different stress levels (approximately 200 MPa for the hard grain and 125 MPa for soft grains at the beginning of hold). At the end of the tensile loading process and the beginning of the hold, the stresses appear quite uniform within grains with sharp stress jumps occurring at the grain boundaries. The relaxation process significantly alters the stress patterns and stress gradients occur within grains. The interaction between neighboring grains that relax at different rates may contribute to the

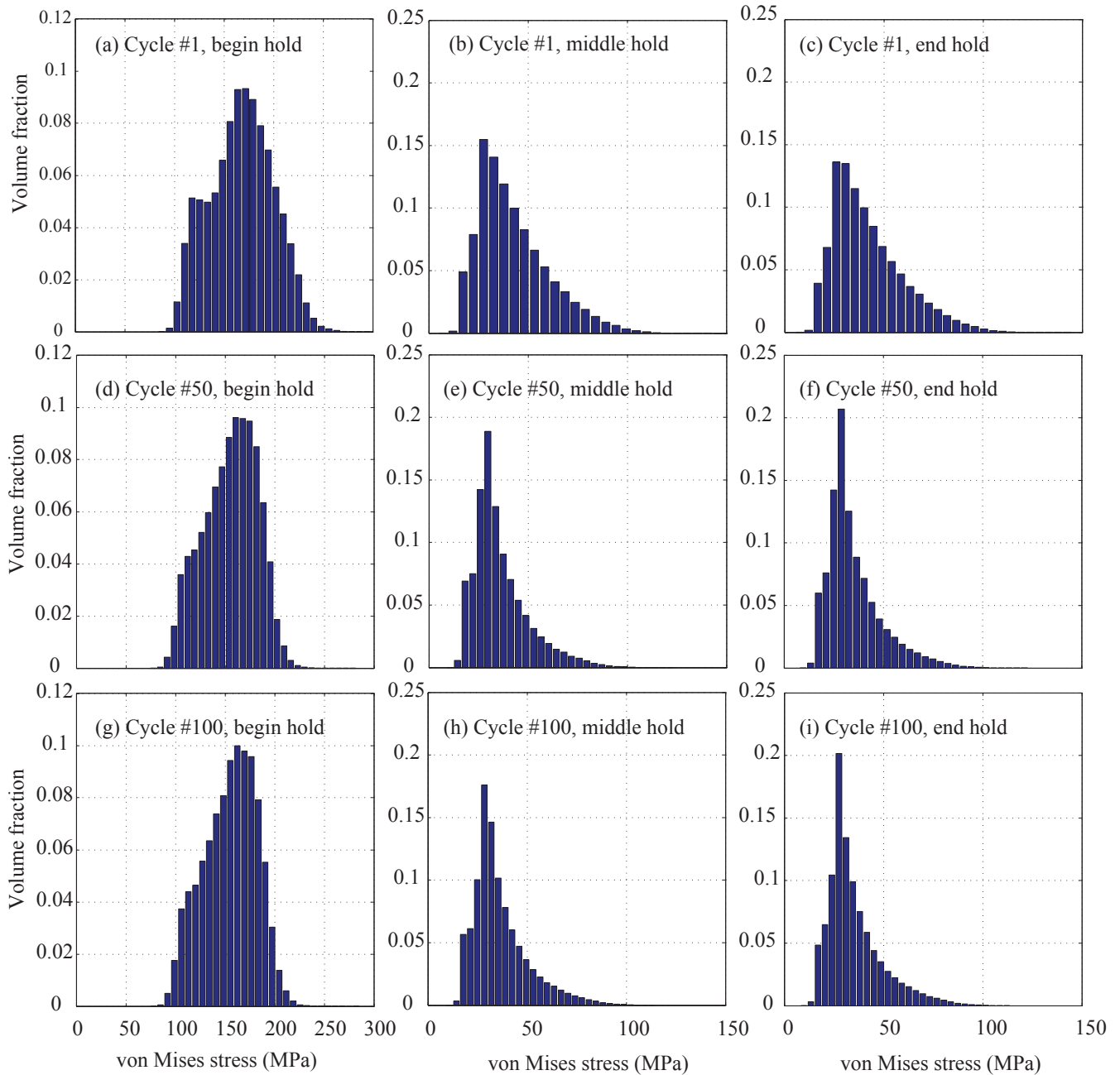


Figure 20: Von Mises stress histograms at different stages within the first (a)-(c), 50th (d)-(e) and 100th (g)-(i) cycle.

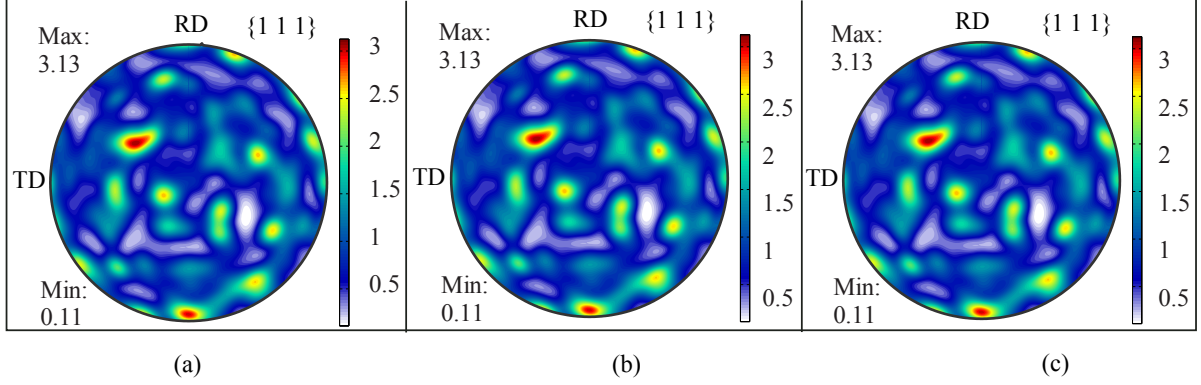


Figure 21: $\{1\ 1\ 1\}$ pole figures of the first cycle: (a) beginning of hold; (b) middle of hold; (c) end of hold.

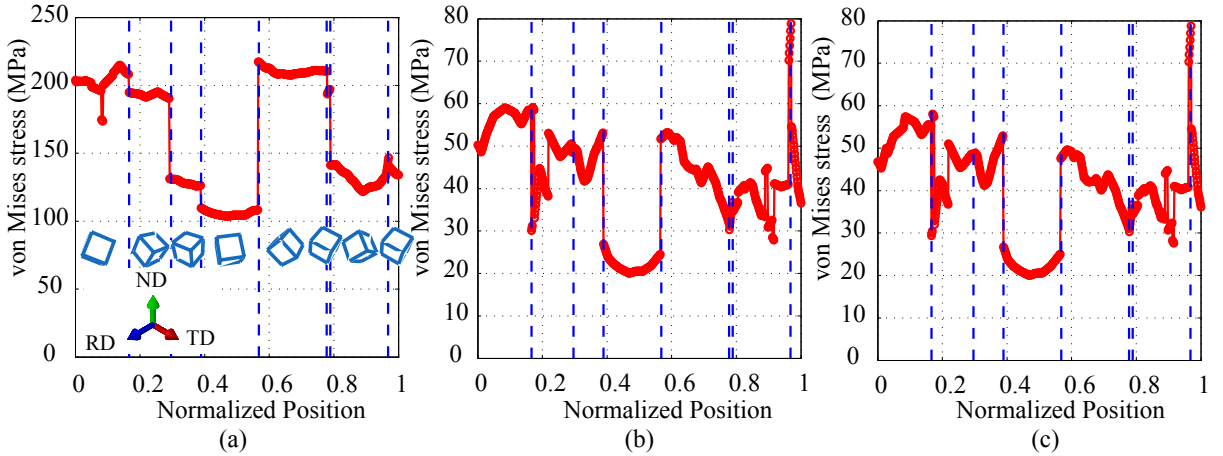


Figure 22: Von Mises stress along a line passing the center of the RVE along X direction of the first cycle: (a) beginning of hold; (b) middle of hold; (c) end of hold.

complex stress distributions observed during the creep fatigue relaxation process. Within a given cycle, a more uniform stress distribution is observed between hard and soft grains at the end of strain hold compared to the beginning of hold. This is because stresses throughout the microstructure asymptotically reduce, due to the viscoplastic relaxation process under constant macroscopic strain. The simulations do not show a noticeably more uniform stress distribution as a function of cycles (i.e., from cycle 1 to 50 to 100). Furthermore, subgrain formation experimentally observed in creep-fatigue behavior of alloy 617 (see e.g., [9]) may be linked to the formation of persistent intragranular stress jumps and gradients.

5 Summary and future research interests

We presented the formulation, implementation and calibration of a CPFE model for nickel-based alloy IN 617 at high temperature. Model formulation, implementation and model parameters calibration are discussed in detail, and verification against a series of fatigue and creep-fatigue tests with different strain ranges and hold times are conducted. The proposed evolution equation for the slip resistance can well capture the stress drop in the first cycle of both fatigue and creep-fatigue tests, as well as the softening reemerging at every cycle after strain hold in the creep-fatigue tests. The current model assumes full traction continuity along grain boundaries while future work will involve cohesive zone modeling of the grain boundaries, which will allow the crack initialization prediction at grain boundaries, and ultimately life prediction. Furthermore, the proposed model will be coupled to structural scale simulations using concurrent-hierarchical multiscale modeling (e.g., [66, 64, 63]), and through sequential multiscale modeling to calibrate model parameters of phenomenological models (e.g., [67, 65]).

6 Acknowledgement

The authors gratefully acknowledge the research funding from the US Department of Energy, Nuclear Energy University Program (Grant No: 62-0476822) and Air Force Office of Scientific Research Multiscale Structural Mechanics and Prognosis Program (Grant No: FA9550-13-1-0104). We acknowledge the technical cooperation with Prof. Yongming Liu at Arizona State University for providing experimental EBSD data for IN 617, and Dr. Richard Wright at Idaho National Laboratory for providing experimental fatigue and creep fatigue data. The authors would also like to acknowledge Dr. Cerrone from Cornell University for sharing his PPM software for microstructure volume mesh generation.

References

- [1] M. Anahid, M. K. Samal, and S. Ghosh. Dwell fatigue crack nucleation model based on crystal plasticity finite element simulations of polycrystalline titanium alloys. *J. Mech. Phys. Solids*, 2011.
- [2] L. Balogh, S. Niezgoda, A. Kanjarla, D. Brown, B. Clausen, W. Liu, and C. Tom. Spatially

resolved in situ strain measurements from an interior twinned grain in bulk polycrystalline AZ31 alloy. *Acta Mater.*, 61:3612–3620, 2013.

- [3] T. Belytschko, W. Liu, B. Moran, and K. Eikhodary. *Nonlinear Finite Elements for Continua and Structures*. John Wiley and Sons, New York, 2nd edition, 2014.
- [4] J. Benz, T. Lillo, and R. Wright. Aging of alloy 617 at 650 and 750 °c. Technical report, Idaho National Laboratory, 2013.
- [5] E. Busso, F. Meissonnier, and N. O'Dowd. Gradient-dependent deformation of two-phase single crystals. *J. Mech. Phys. Solids*, 48:2333–2361, 2000.
- [6] E. P. Busso and F. A. McClintock. A dislocation mechanics-based crystallographic model of a B2-type intermetallic alloy. *Int. J. Plast.*, 12:1–28, 1996.
- [7] R. Carmona, Q. Zhu, C. Sellars, and J. Beynon. Controlling mechanisms of deformation of AA5052 aluminium alloy at small strains under hot working conditions. *Mater. Sci. Eng. A*, 393:157–163, 2005.
- [8] L. Carroll. Creep-fatigue behavior of alloy 617 at 850 and 950°C. Technical report, Idaho National Laboratory, 2015.
- [9] M. Carroll and L. Carroll. Developing dislocation subgrain structures and cyclic softening during high-temperature creepfatigue of a Nickel alloy. *Metall. Trans. A*, 44:3592–3607, 2013.
- [10] L. Carrolla, C. Cabetb, M. Carrolla, and R. Wright. The development of microstructural damage during high temperature creepfatigue of a nickel alloy. *Int. J. Fatigue*, 47:115–125, 2013.
- [11] A. Cerrone, J. Tucker, C. Stein, A. Rollett, and A. Ingraffea. Micromechanical modeling of RENE88DT:from characterization to simulation. In *Proceedings of the 2012 Joint Conference of the Engineering Mechanics Institute and the 11th ASCE Joint Specialty Conference on Probabilistic Mechanics and Structural Reliability*, 2012.
- [12] J. Chaboche. Constitutive equations for cyclic plasticity and cyclic viscoplasticity. *Int. J. Plast.*, 5:247–302, 1989.

- [13] X. Chen, M. A. Sokolov, S. Sham, D. L. E. III, J. T. Busby, K. Mo, and J. F. Stubbins. Experimental and modeling results of creep-fatigue life of Inconel 617 and Haynes 230 at 850 °C. *J. Nucl. Mater.*, 432:94–101, 2013.
- [14] J. Cheng and S. Ghosh. A crystal plasticity FE model for deformation with twin nucleation in magnesium alloys. *Int. J. Plast.*, 67:148–170, 2015.
- [15] J. Christian and S. Mahajan. Deformation twinning. *Prog. Mater. Sci.*, 39:1–157, 1995.
- [16] M. Geers, M. Cottura, B. Appolaire, E. Busso, S. Forest, and A. Villani. Coupled glide-climb diffusion-enhanced crystal plasticity. *J. Mech. Phys. Solids*, 70:136 – 153, 2014.
- [17] M. Groeber and M. Jackson. DREAM.3D: A digital representation environment for the analysis of microstructure in 3D. *Integr. Mater. Manuf. Innov.*, 3:5–19, 2014.
- [18] R. Hill and J. Rice. Constitutive analysis of elastic-plastic crystals at arbitrary strain. *J. Mech. Phys. Solids*, 20:401–413, 1972.
- [19] S. R. Kalidindi. Incorporation of deformation twinning in crystal plasticity models. *J. Mech. Phys. Solids*, 46:267–290, 1998.
- [20] W.-G. Kim, S.-N. Yin, J.-Y. Park, S.-D. Hong, and Y.-W. Kim. An improved methodology for determining tensile design strengths of alloy 617. *J. Mech. Sci. Technol.*, 26:379–387, 2012.
- [21] M. Knezevic, A. Levinson, R. Harris, R. Mishra, R. Doherty, and S. Kalidindi. Deformation twinning in AZ31: Influence on strain hardening and texture evolution. *Acta Mater.*, 58:6230–6242, 2010.
- [22] M. Kothari and L. Anand. Elasto-viscoplastic constitutive equations for polycrystalline metals: Application to tantalum. *J. Mech. Phys. Solids*, 46:51–83, 1998.
- [23] R. A. Lebensohn, C. S. Hartley, C. N. Tome, and O. Castelnau. Modeling the mechanical response of polycrystals deforming by climb and glide. *Philos. Mag.*, 90:567–583, 2010.
- [24] B. Lin, L. Zhao, J. Tong, and H. Christ. Crystal plasticity modeling of cyclic deformation for a polycrystalline nickel-based superalloy at high temperature. *Mater. Sci. Eng. A*, 527:3581–3587, 2010.

- [25] A. Ma and F. Roters. A constitutive model for FCC single crystals based on dislocation densities and its application to uniaxial compression of aluminium single crystals. *Acta Mater.*, 52:3603–3612, 2004.
- [26] W. Mankins, J. Hosier, and T. Bassford. Microstructure and phase stability of inconel alloy 617. *Metall. Trans.*, 5:2579–2590, 1974.
- [27] E. Marin and P. Dawson. On modelling the elasto-viscoplastic response of metals using polycrystal plasticity. *Comput. Methods Appl. Mech. Engrg.*, 165:1–21, 1998.
- [28] E. B. Marin. On the formulation of a crystal plasticity model. Technical report, Sandia National Laboratories, 2006.
- [29] S. D. Martino, R. Faulkner, S. Hogg, S. Vujic, and O. Tassa. Characterisation of microstructure and creep properties of alloy 617 for high-temperature applications. *Mater. Sci. Eng. A*, 619:77–86, 2014.
- [30] K. Mo. *Microstructural Evolution and Mechanical Behavior in Nickel based Alloy for Very High Temperature Reactor*. PhD thesis, University of Illinois at Urbana-Champaign, 2011.
- [31] K. Mo, G. Lovicu, X. Chen, H.-M. Tung, J. B. Hansen, and J. F. Stubbins. Mechanism of plastic deformation of a ni-based superalloy for VHTR applications. *J. Nucl. Mater.*, 441:695 – 703, 2013.
- [32] K. Mo, G. Lovicu, H.-M. Tung, X. Chen, Y. Miao, J. B. Hansen, and J. F. Stubbins. Effect of orientation on plastic deformations of alloy 617 for VHTR applications. *J. Nucl. Mater.*, 443:366–377, 2013.
- [33] S. Q. Nazrul Islam and T. Hassan. A unified constitutive model for high temperature multiaxial creep-fatigue and ratcheting response simulation of alloy 617. In *ASME Proceedings 22nd Scavuzzo Student Paper Symposium and Competition*, 2014.
- [34] D. Peirce, R. Asaro, and A. Needleman. An analysis of nonuniform and localized deformation in ductile single crystals. *Acta Metall.*, 30:1087–1119, 1982.
- [35] D. Peirce, R. Asaro, and A. Needleman. Material rate dependence and localized deformation in crystalline solids. *Acta Metall.*, 31:1951–1976, 1983.

- [36] H. Pottebohm, G. Neite, and E. Nembach. Elastic properties (the stiffness constants, the shear modulus and the dislocation line energy and tension) of Ni-Al solid solutions and of the nimonic alloy PE16. *Mater. Sci. Eng. A*, 60:189–194, 1983.
- [37] M. Powell. A fast algorithm for nonlinearly constrained optimization calculations. In G. Watson, editor, *Numerical Analysis*, volume 630 of *Lecture Notes in Mathematics*, pages 144–157. Springer Berlin Heidelberg, 1978.
- [38] P. Pritchard, L. Carroll, and T. Hassan. Constitutive modeling of high temperature uniaxial creep-fatigue and creep-ratcheting responses of alloy 617. In *Proceedings of the ASME 2013 Pressure Vessels and Piping Conference*, 2013.
- [39] C. Rasmussen and C. Williams. *Gaussian Processes for Machine Learning*. Springer, New York, 2006.
- [40] W. Ren and R. W. Swindeman. A review on current status of alloys 617 and 230 for Gen IV nuclear reactor internals and heat exchangers. *ASME. J. Pressure Vessel Technol.*, 131, 2009.
- [41] D. Robinson. Constitutive relationships for anisotropic high-temperature alloys. *Nucl. Eng. Des.*, 83:389–396, 1984.
- [42] F. Roters, P. Eisenlohr, L. Hantcherli, D. Tjahjanto, T. Bieler, and D. Raabe. Overview of constitutive laws, kinematics, homogenization and multiscale methods in crystal plasticity finite-element modeling: Theory, experiments, applications. *Acta Mater.*, 58:1152–1211, 2010.
- [43] T.-L. Sham and K. P. Walker. Preliminary development of a unified viscoplastic constitutive model for alloy 617 with special reference to long term creep behavior. In *ASME Proceedings, Materials and Components*, 2008.
- [44] M. Shenoy, A. Gordon, D. McDowell, and R. Neu. Thermomechanical fatigue behavior of a directionally solidified Ni-base superalloy. *J. Eng. Mater. Technol.*, 127:325–336, 2005.
- [45] O. Sherby and P. Burke. Mechanical behavior of crystalline solids at elevated temperature. *Prog. Mater. Sci.*, 13:323–390, 1968.

- [46] Y. Shi, K. Yuan, X. Zhao, and Y. Wu. Study on comparison between Inconel 617 and Gh3128 as structural material candidates for intermediate heat exchanger. In *Proceedings of the 2013 21st International Conference on Nuclear Engineering ICONE21*. ASME, 2013.
- [47] E. Taleff, W. Green, M.-A. Kulas, T. R. McNelley, and P. Krajewski. Analysis, representation, and prediction of creep transients in class I alloys. *Mater. Sci. Eng. A*, 410-411: 32–37, 2005.
- [48] G. Taylor. Plastic Strain in Metals. *J. Inst. Met.*, 62:307–324, 1938.
- [49] T. C. Totemeier, H. Tian, D. E. Clark, and J. A. Simpson. Microstructure and strength characteristics of alloy 617 welds. Technical report, Idaho National Laboratory, 2005.
- [50] H. Turkmen, P. Dawson, and M. Miller. The evolution of crystalline stresses of a polycrystalline metal during cyclic loading. *Int. J. Plast.*, 18:941–969, 2002.
- [51] X. Wen. *Creep Behavior of High Temperature Alloys for Generation IV Nuclear Energy Systems*. PhD thesis, University of Cincinnati, 2014.
- [52] J. Wright, J. Simpson, R. Wright, L. Carroll, and T. Sham. Strain rate sensitivity of alloys 800h and 617. In *Proceedings of the 2013 ASME Pressure Vessels & Piping Conference*, Paris, France, 2013.
- [53] J. K. Wright, L. J. Carroll, C. Cabet, T. M. Lillo, J. Benz, J. A. Simpson, W. R. Lloyd, J. A. Chapman, and R. N. Wright. Characterization of elevated temperature properties of heat exchanger and steam generator alloys. *Nucl. Eng. Des.*, 251:252–260, 2012.
- [54] J. K. Wright, L. J. Carroll, J. A. Simpson, and R. N. Wright. Low cycle fatigue of alloy 617 at 850°C and 950°C. *J. Eng. Mater. Technol.*, 135:031005, 2013.
- [55] J. K. Wright, N. J. Lybeck, and R. N. Wright. Tensile properties of alloy 617 bar stock. Technical report, Idaho National Laboratory, 2013.
- [56] M. Yoo and J. Lee. Deformation twinning in h.c.p. metals and alloys. *Phil. Mag. A*, 63: 987–1000, 1991.

- [57] K.-. Zhang, J. Ju, Z. Li, Y.-L. Bai, and W. Brocks. Micromechanics based fatigue life prediction of a polycrystalline metal applying crystal plasticity. *Mech. Mater.*, 85:16–37, 2015.
- [58] M. Zhang, J. Zhang, and D. McDowell. Microstructure-based crystal plasticity modeling of cyclic deformation of Ti-6Al-4V. *Int. J. Plast.*, 23:1328–1348, 2007.
- [59] J.C. Stinville, N. Vanderesse, F. Bridier, P. Bocher, and T.M. Pollock. High resolution mapping of strain localization near twin boundaries in a nickel-based superalloy. *Acta Mater.*, 98:29–42, 2015.
- [60] J.C. Stinville, W.C. Lenthe, J. Miao, and T.M. Pollock. A combined grain scale elasticplastic criterion for identification of fatigue crack initiation sites in a twin containing polycrystalline nickel-base superalloy. *Acta Mater.*, 103:461–473, 2016.
- [61] U. F. Kocks, C. N. Tome, and H. R. Wenk. *Texture and Anisotropy: Preferred Orientations in Polycrystals and Their Effect on Materials Properties*. Cambridge University Press, Cambridge, 1998.
- [62] S. Zhang and C. Oskay. Variational multiscale enrichment method with mixed boundary conditions for elasto-viscoplastic problems. *Comput. Mech.*, 55:771–787, 2015.
- [63] S. Zhang and C. Oskay. Reduced order variational multiscale enrichment method for elasto-viscoplastic problems. *Comput. Methods Appl. Mech. Engg.*, 300:199–224, 2016.
- [64] X. Zhang and C. Oskay. Eigenstrain based reduced order homogenization for polycrystalline materials. *Comput. Methods Appl. Mech. Engg.*, 297:408–436, 2015.
- [65] H. Yan and C. Oskay. A viscoelasticviscoplastic model of titanium structures subjected to thermo-chemo-mechanical environment. *Int. J. Solids Struct.*, 5657:29–42, 2015.
- [66] C. Oskay. Variational multiscale enrichment for modeling coupled mechano-diffusion problems. *Int. J. Numer. Methods Eng.*, 89(6):686–705, 2012.
- [67] C. Oskay and M. Haney. Computational modeling of titanium structures subjected to thermo-chemo-mechanical environment. *Int. J. Solids Struct.*, 47(24):3341–3351, 2010.

- [68] M. J. Bogdanor, S. Mahadevan, and C. Oskay. Uncertainty quantification in damage modeling of heterogeneous materials. *Int. J. Multisc. Comp. Eng.*, 11:289–307, 2013.